

Durham Research Online

Deposited in DRO:

27 June 2018

Version of attached file:

Published Version

Peer-review status of attached file:

Peer-reviewed

Citation for published item:

Alton, P. D. and Smith, R. J. and Lucey, J. R. (2018) 'KINETyS II : constraints on spatial variations of the stellar initial mass function from K-band spectroscopy.', *Monthly notices of the Royal Astronomical Society.*, 478 (4). pp. 4464-4486.

Further information on publisher's website:

<https://doi.org/10.1093/mnras/sty1242>

Publisher's copyright statement:

This article has been accepted for publication in *Monthly Notices of the Royal Astronomical Society* ©: 2018 The Author(s) Published by Oxford University Press on behalf of the Royal Astronomical Society. All rights reserved.

Additional information:

Use policy

The full-text may be used and/or reproduced, and given to third parties in any format or medium, without prior permission or charge, for personal research or study, educational, or not-for-profit purposes provided that:

- a full bibliographic reference is made to the original source
- a [link](#) is made to the metadata record in DRO
- the full-text is not changed in any way

The full-text must not be sold in any format or medium without the formal permission of the copyright holders.

Please consult the [full DRO policy](#) for further details.

KINeTyS II: Constraints on spatial variations of the stellar initial mass function from *K*-band spectroscopy

P. D. Alton,[★] R. J. Smith[★] and J. R. Lucey

Centre for Extragalactic Astronomy, Department of Physics, Durham University, South Road, Durham DH1 3LE, UK

Accepted 2018 May 4. Received 2018 April 7; in original form 2017 July 12

ABSTRACT

We investigate the spatially resolved stellar populations of a sample of seven nearby massive early-type galaxies (ETGs), using optical and near-infrared data, including *K*-band spectroscopy. This data offers good prospects for mitigating the uncertainties inherent in stellar population, modelling by making a wide variety of strong spectroscopic features available. We report new *K*-band Multi-Object Spectrograph (KMOS) measurements of the average empirical radial gradients out to the effective radius in the strengths of the CaI 1.98 and 2.26 μm features, the NaI 2.21 μm line, and the CO 2.30 μm bandhead. Following previous work, which has indicated an excess of dwarf stars in the cores of massive ETGs, we pay specific attention to radial variations in the stellar initial mass function (IMF) as well as modelling the chemical abundance patterns and stellar population ages in our sample. Using state-of-the-art stellar population models, we infer an [Fe/H] gradient of -0.16 ± 0.05 per dex in fractional radius and an average [Na/Fe] gradient of -0.35 ± 0.09 . We find a large but radially constant enhancement to [Mg/Fe] of ~ 0.4 and a much lower [Ca/Fe] enhancement of ~ 0.1 . Finally, we find no significant IMF radial gradient in our sample on average and find that most galaxies in our sample are consistent with having a Milky Way-like IMF, or at most a modestly bottom heavy IMF (e.g. less dwarf enriched than a single power-law IMF with the Salpeter slope).

Key words: stars: luminosity function, mass function – galaxies: abundances – galaxies: elliptical and lenticular, cD – galaxies: stellar content.

1 INTRODUCTION

When studying an evolved population of stars, one of the key assumptions made concerns the form of the stellar initial mass function (IMF). The IMF – the initial distribution of stellar masses in a newly formed stellar population – determines the future chemical evolution of the host galaxy, the rate of supernova explosions, and a variety of key observables. These include, critically, the mass-to-light ratio (M/L) of the stellar population; any calculation of the stellar mass contained in a galaxy therefore depends on the IMF.

In our own galaxy, methods based on direct counting of stars have revealed that the IMF is remarkably uniform despite variations in environmental conditions (e.g. as reviewed by Bastian, Covey & Meyer 2010) with few exceptions (see e.g. Luhman et al. 2003, Marks et al. 2012). Above $1 M_{\odot}$, the IMF is well described by a power law (Salpeter 1955), and at lower masses, this power law turns over (see Kroupa 2001; Chabrier 2003). Nevertheless, it is

unclear whether the IMF in other galaxies has a similar functional form.

In unresolved stellar populations constraining the IMF is challenging, but attempts to do so have met with a certain amount of success in recent years. A key result has been the measurement, using multiple different techniques, of IMF variations in massive early-type galaxies (ETGs). In these galaxies the IMF appears to be ‘bottom-heavy’, meaning that their stellar populations contain a larger fraction of dwarf stars than those in the Milky Way: this can increase the M/L of these galaxies by as much as a factor of 2.

Some methods yielding bottom-heavy IMFs in ETGs arrive at the result indirectly, via constraints on the M/L ratio from gravitational lensing (e.g. Auger et al. 2010, but see also Smith & Lucey 2013) or dynamics (e.g. Cappellari et al. 2012), or both (Thomas et al. 2011). There are alternative interpretations of enhanced M/L ratios: variations in the high-mass end of the IMF can also increase the M/L of an old stellar population due to the inclusion of more dim stellar remnants and variations in the dark-matter content of a galaxy can also play a role in some cases.

An alternative, spectroscopic class of methods provides direct support for the bottom-heavy interpretation. Such methods in-

[★] E-mail: padraig.alton@durham.ac.uk (PDA); russell.smith@durham.ac.uk (RJS)

volve fitting models to galaxy spectra. Certain spectral features are strong/weak in the spectra of dwarf/giant stars (or vice versa) with the same surface temperature, chemical composition, and age. In old stellar populations, the strength of these features therefore provides information about the relative contribution to the total light from dwarf and giant stars.

These methods have been used by, amongst others, Conroy & van Dokkum (2012b, hereafter CvD12b), Smith, Lucey & Carter (2012), Spiniello et al. (2012), La Barbera et al. (2013), Martín-Navarro et al. (2015), and van Dokkum et al. (2017) to infer bottom-heavy IMFs in the most massive ETGs, although this result has been challenged by e.g. Zieleniewski et al. (2015), McConnell, Lu & Mann (2016), and Vaughan et al. (2018).

Spectroscopic models suffer from degeneracies between different properties, e.g. a feature sensitive to the IMF will also be sensitive to the abundance of one or more chemical elements. Simultaneous consideration of a wide variety of spectral features with different sensitivities to the underlying properties of the stellar population can break these degeneracies. Measurements of near-infrared features have begun to play a larger role in studies of this type: this wavelength regime contains a plethora of useful features, as outlined in Conroy & van Dokkum (2012a, hereafter CvD12a). Moreover, advances in instrumentation and the development of empirical stellar spectral libraries at longer wavelengths (e.g. Rayner, Cushing & Vacca 2009) allow much more accurate measurement and modelling of these features than has previously been possible. Recent examples include McConnell et al. (2016), La Barbera et al. (2016), van Dokkum et al. (2017), Vaughan et al. (2018), and Zieleniewski et al. (2017), as well as the first paper in this series, Alton, Smith & Lucey (2017, hereafter Paper I).

Particular attention has been paid in these studies to spatial variations in the form of the IMF. ETGs are thought to assemble most of their stellar mass rapidly in a (swiftly quenched) starburst phase at $z \sim 2-3$, before evolving passively through dry minor mergers. Observations indicate that during this latter phase, ETGs greatly increase in size (e.g. Bezanson et al. 2009, Hopkins et al. 2009, Hopkins et al. 2010), a picture supported by simulations (e.g. Oser et al. 2010, 2012; Hilz, Naab & Ostriker 2013). Thus, the stellar populations in the outskirts of ETGs have a different physical origin than those in the core (where, due to signal-to-noise (S/N) constraints, most existing observations have been made) and may, therefore, also be formed according to a different IMF. To date, however, the observational picture remains ambiguous, with Martín-Navarro et al. (2015), La Barbera et al. (2016), and van Dokkum et al. (2017) finding evidence for radial variations in the IMF in a number of ETGs, whilst in the works of Vaughan et al. (2018), Zieleniewski et al. (2017), and Paper I, no clear evidence is found.

The KMOS Infrared Nearby Early-Type Survey (KINeTyS) is an investigation of the stellar population properties (principally ages, chemical abundances, and underlying IMF) of nearby ETGs, with a particular focus on radial variations of these properties. In the first KINeTyS paper (i.e. Paper I), we presented VLT-KMOS spectra covering the 0.78–1.34 μm range for a sample of eight nearby ETGs. Through measurements of a variety of spectral indices, in concert with archival optical data for the targets from the ATLAS^{3D} survey (McDermid et al. 2015), we inferred radial stellar population gradients. By stacking spectra, we were able to track the average gradients for the sample out to the effective radius. We found some strong chemical abundance gradients (e.g. $[\alpha/\text{H}] = -0.20 \pm 0.01$, $[\text{Na}/\text{H}] = -0.53 \pm 0.07$) but did not find evidence for radial IMF variations (variations in the fractional contribution of dwarf stars to

the light were limited to a few per cent at most), and were unable to constrain the abundances of some elements and stellar population age.

In this paper, we extend the work presented in Paper I by measuring a set of gravity-sensitive spectroscopic features in the *K* band. In principle, this can further mitigate the degeneracies inherent in stellar population modelling whilst also facilitating a comparison of models and data in this interesting yet still less-well-explored wavelength regime. Whilst studies of the IMF rooted in infrared spectroscopy are becoming more common, there remains a great deal of less-explored territory at longer wavelengths ($> 1 \mu\text{m}$). Spectroscopic models indicate that this regime is no-less promising than the more commonly studied bands (e.g. see CvD12a), containing a multitude of strong absorption features with dependencies on a variety of stellar population properties.

In this work, we deploy a more sophisticated approach to stellar population inference. We use an updated set of stellar population models, which are based on the updated IRTF library of Villaume et al. (2017) and are described in full in Conroy et al. (2018). These models use a more comprehensive set of stellar population parameters than the models of Paper I. Hereafter, we refer to these as the CvD16 models, and to those used in Paper I as the CvD12 models.

The paper is organized as follows. In Section 2, we present new *K*-band data from the KINeTyS sample. In Section 3, we describe our procedures for measuring the strengths of various spectroscopic features. In Section 4, we present measurements of empirical spectroscopic gradients for *K*-band features in the KINeTyS sample and compare these with predictions from the models of Paper I. In Section 5, we give details of our updated methods for stellar population inference and present results thereby derived for the KINeTyS sample. We discuss all our results in Section 6 and give our conclusions in Section 7.

2 DATA

2.1 Observations

Seven of the eight nearby ETGs introduced in Paper I were re-observed with KMOS (Sharples et al. 2013) in the *K* band (1.93–2.50 μm) using the same ‘sparse mosaic’ observing strategy as in that work (see Fig. 1, Paper I). The data were obtained between 2016 February 20 and August 8 [run ID: 097.B-0882(A), PI: Alton]. Sample details are given in Table 1. In the *K* band, KMOS has resolving power $R = 4200$. For most targets, we took 6×480 s exposures on each pointing, resulting in a total on-source integration time of 2880 s (for NGC 1407 and NGC 4621, it was only possible to take half as many exposures, for a total of 1440 s on-source). The S/N ranges from > 200 per pixel for the innermost region of the galaxies, falling to ~ 10 at the effective radius (so those data are only useful when combined across the sample).

2.2 Data reduction

The KMOS data were reduced mostly as in Paper I, using a slightly modified version of the European Southern Observatory (ESO) standard pipeline. However, we modified the atmospheric absorption correction procedure with the MOLECFIT (v1.0.2) tool. To achieve optimal performance, we separately fit the atmosphere in two wavelength ranges, 19587–21075 and 21075–23964 Å, modelling H₂O, CH₄, and CO₂ absorption. The first of these ranges contains strong,

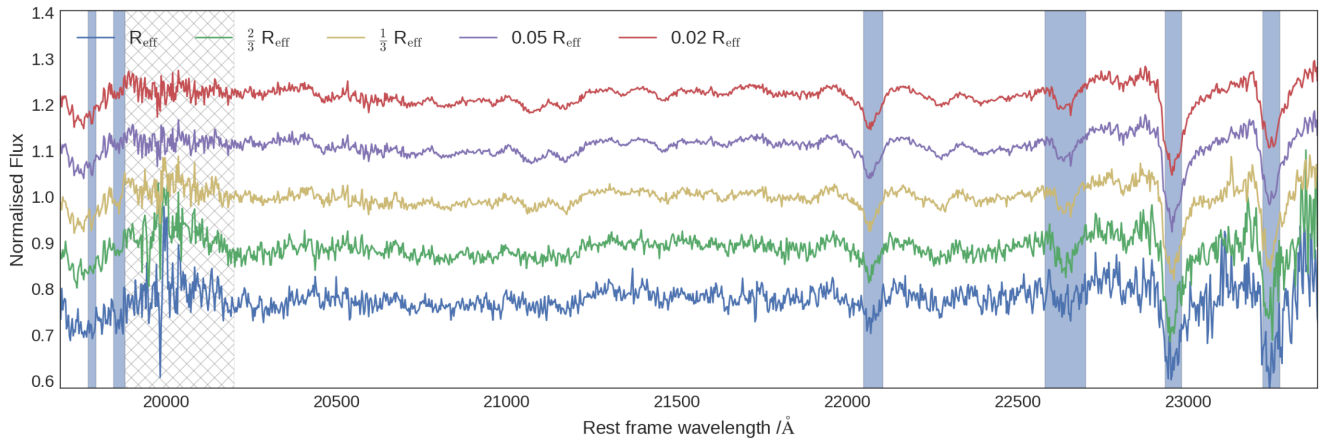


Figure 1. *K*-band spectra from KMOS, median-stacked at fixed fraction of the effective radius. Even in the outlying regions of the galaxy, the signal of the strong absorption features are recovered via this method. The hatched region shows a region of particularly strong telluric absorption (atmospheric transmission $\lesssim 50$ per cent). The features listed in Table 2 are shown by the light blue bands.

Table 1. List of sample galaxies with observation details and key properties listed. Effective radii and total (*J*-band) magnitudes within the effective radius were extracted from 2MASS *J*-band images and used to calculate the mean surface brightness. Recession velocities were derived using pPXF and $\sigma(R_{\text{eff}}/8)$ values and fast/slow rotator status was taken from the ATLAS 3D survey (except for NGC 1407 for which a value was derived from our pPXF fits). Relative M/L taken from CvD12b.

Name	Seeing (arcsec)	Observation		R_{eff} (arcsec)	<i>cz</i> (km s ⁻¹)	$\sigma(R_{\text{eff}}/8)$ (km s ⁻¹)	Surface brightness (mag _J arcsec ⁻²)	Relative M/L (Milky Way = 1)	Ellipticity	Notes
		time (s)								
NGC 1407	0.68–0.75	1440		36.2	1950	301	17.4	–	0.00	Slow rotator
NGC 3377	0.88–1.16	2880		23.3	690	146	17.0	1.16	0.40	Fast rotator
NGC 3379	0.95–1.24	2880		28.5	900	213	16.5	1.60	0.00	Fast rotator
NGC 4486	0.99–1.34	2880		44.5	1290	314	16.9	1.90	0.00	Slow rotator
NGC 4552	0.89–1.07	2880		24.1	390	262	16.6	2.04	0.00	Slow rotator
NGC 4621	1.02–1.22	1440		27.7	480	224	16.8	1.96	0.33	Fast rotator
NGC 5813	1.13–1.57	2880		33.7	1920	226	17.9	1.37	0.25	Slow rotator

broad absorption by CO₂ which makes it difficult to fit a polynomial continuum through this range. Splitting the fit into two (largely independent) segments prevents this issue from affecting the redder part of the spectrum, where most of the stellar features are of interest.

We improve our methods from Paper I by characterizing the variability of the atmospheric correction in each observing run, i.e. over six exposures (at each wavelength we estimate the 68 per cent scatter between the set of six applied corrections). This likely represents an overestimate of the error (since, in reality, we expect that the atmospheric absorption profile will vary between observations, rather than differences being entirely due to observational uncertainties/scatter). Nevertheless we propagate this additional uncertainty to later reduction steps.

As before, spectra from the same radial extraction region were, for each galaxy, combined to create a single 1D spectrum for each physical region of the galaxy probed. This was accomplished by

first dividing out continuum variations, then median-stacking the spectra.

2.3 Velocity dispersions and index measurements

In order to correct our measurements to a common velocity dispersion, we made use of the redshifts and velocity dispersions derived in Paper I. We note that for spectra with such high intrinsic velocity dispersion, the difference in instrumental broadening between bands has a negligible effect, increasing the total velocity dispersion by < 10 km s⁻¹ and hardly affecting the correction of the index strengths.

Table 2 describes all spectral features considered in this work. This set of indices includes three optical features, for which we use archival ATLAS^{3D} measurements presented in McDermid et al. (2015) – these are essential for providing good constraints on [Fe/H] and strengthen constraints on other properties. In addition, we make

Table 2. List of absorption index names and definitions (vacuum wavelength definitions, given in Å); originally from CvD12a.

Index name	Blue continuum	Feature definition	Red continuum	Notes
H β	4827.9–4847.9	4847.9–4876.6	4876.6–4891.6	ATLAS ^{3D} data
Fe 5015 Å	4946.5–4977.8	4977.8–5054.0	5054.0–5065.3	
Mgb	5142.6–5161.4	5160.1–5192.6	5191.4–5206.4	
Na I (0.82 μ m)	8170.0–8177.0	8177.0–8205.0	8205.0–8215.0	Paper I data
Ca II (0.86 μ m a)	8484.0–8513.0	8474.0–8484.0	8563.0–8577.0	
Ca II (0.86 μ m b)	8522.0–8562.0	8474.0–8484.0	8563.0–8577.0	
Ca II (0.86 μ m c)	8642.0–8682.0	8619.0–8642.0	8700.0–8725.0	
Mg I (0.88 μ m)	8801.9–8816.9	8777.4–8789.4	8847.4–8857.4	
FeH (0.99 μ m)	9905.0–9935.0	9855.0–9880.0	9940.0–9970.0	
Ca I (1.03 μ m)	10337–10360	10300–10320	10365–10390	
Na I (1.14 μ m)	11372–11415	11340–11370	11417–11447	
K I (1.17 μ m a)	11680–11705	11667–11680	11710–11750	
K I (1.17 μ m b)	11765–11793	11710–11750	11793–11810	
K I (1.25 μ m)	12505–12545	12460–12495	12555–12590	New KMOS data
Al I (1.31 μ m)	13115–13165	13090–13113	13165–13175	
Ca I (1.98 μ m a)	19740–19765	19770–19795	19800–19840	
Ca I (1.98 μ m b)	19800–19840	19845–19880	19885–19895	
Na I (2.21 μ m)	22035–22045	22047–22105	22107–22120	
Ca I (2.26 μ m)	22500–22575	22580–22700	22705–22780	
CO (2.30 μ m a)	22860–22910	22932–22982	23020–23070	
CO (2.30 μ m b)	23150–23200	23220–23270	23300–23350	

use of the index measurements presented in Paper I. Finally, for each spectrum, we measured the equivalent widths of a set of *K*-band spectral indices.

For each feature, we used the flux uncertainties to create a set of Monte Carlo realizations of our spectra from which the uncertainties of these index measurements could be inferred. The measured velocity dispersions were used to correct all index measurements to 230 km s^{−1}; the uncertainty on these corrections was also propagated. All measured equivalent widths and uncertainties are given in Appendix A (Tables A1–A7).

2.4 Stacked spectra

As in Paper I we chose to make use of stacked spectra in our analysis, creating these by the same method as before (described below). This has a number of advantages, the most important being that stacking spectra with slightly different redshifts in the source rest-frame suppresses any systematics introduced in the observed rest frame (e.g. due to poor subtraction of sky emission lines or sub-par telluric corrections). Additionally, stacked spectra can be used to constrain the average behaviour of the sample (and, in turn, this can be used to identify unusual objects that deviate from this average).

For the centrally extracted KMOS spectra, the stacking procedure was as follows: we shifted the input spectra into the rest frame and binned them on to a common wavelength grid. We characterized the relative continuum variation by dividing each spectra by the mean spectrum and fitting a sixth order polynomial to the ratio of the two. This relative continuum variation was then divided out and the median flux at each wavelength was evaluated. Errors were created by bootstrap resampling of the input spectra (since the scatter between galaxies is larger than the statistical uncertainty on any given spectrum).

We divided the other KMOS spectra by the centrally extracted spectrum prior to stacking, so that we stacked the *radial variations* of the spectra. We then multiplied these ‘variation stacks’ by the stacked spectrum already derived from the central extraction region. This procedure maximizes the radial variation signal: any constant offset in the strength of spectral features between different galaxies in the stack is divided out.

The KMOS *K*-band spectra are shown in Fig. 1. We measured equivalent widths and statistical uncertainties of available spectroscopic features just as for the spectra of individual galaxies. These measurements are also provided in Appendix A (see Table A8).

3 SPECTROSCOPIC RADIAL GRADIENTS

3.1 Interpretation of absorption line strengths

As outlined in the Introduction section, absorption features in stellar population spectra encode information about the properties of the stars as well as kinematic information (recession velocities, velocity broadening). The strength of those spectral features in the light of individual stars depends on the chemical composition, age, and surface gravity of the star. Because of these dependences, it is in principle possible to constrain the chemical abundance pattern, population age, and relative contribution of dwarf and giant stars to the total light (and thus the IMF).

We present the strengths of four *K*-band features (definitions are given in Table 2) in seven ETGs at five radial locations. These features are as follows.

3.1.1 Ca I 1.98 μ m

The comparatively weak Ca I doublet is principally sensitive to Ca abundance and the IMF, becoming stronger as Ca abundance increases and as the IMF becomes more bottom-heavy. This feature

was first highlighted in [CvD12a](#) as an IMF-sensitive index with the potential to help constrain the shape of the low-mass IMF, but to our knowledge has not been measured before. In Appendix B, we show that (given other constraints on f_{dwarf}) Ca I 1.98 μm can indeed provide information about the IMF shape. This feature lies next to a band of strong telluric absorption and so in some cases is difficult to measure with precision.

3.1.2 Na I 2.21 μm

This strong feature is, in principle, extremely useful for constraining [Na/Fe], since its sensitivity to the IMF is comparatively limited, in contrast to the Na I lines at 0.82 and 1.14 μm . Previous work ([Smith et al. 2015b](#) and see also [Paper I](#)) has indicated that in the CvD12 models, the strengths of these lines are in tension with each other, given other constraints. The measurement of other strong Na features may help to resolve this tension: although the optical Na I 0.59 μm line would be more readily measurable and even less sensitive to the IMF, the Na I 2.21 μm line can none the less provide a valuable constraint. Like the 0.82 and 1.14 μm lines, Na I 2.21 μm is unaffected by interstellar absorption from dust and gas.

This feature has been studied previously at an empirical level in non-spatially resolved spectra by [Silva, Kuntschner & Lyubenova \(2008\)](#) and [Mármol-Queraltó et al. \(2009\)](#). Although at the time accurate, SSP models were not available in the *K* band, Na I 2.21 μm was noted to correlate strongly and positively with galaxy velocity dispersion and also to be very strong in comparison to measurements of Milky Way stars. This latter result was also found by [Davidge, Beck & McGregor \(2008\)](#), in which radial variations of this feature in the central 1 arcsec of compact elliptical galaxies were studied. [Meneses-Goytia et al. \(2015\)](#) compared these strengths with new *K*-band SSP models, confirming that these generally predicted lower strengths for Na I 2.21 μm than had been measured. A more recent treatment by [La Barbera et al. \(2017\)](#) using a new version of the MILES SSP models studied this and other Na features in the optical and near-infrared, finding that the strength of the feature could only be reproduced by a combination of Na superabundance and a bottom-heavy IMF.

3.1.3 Ca I 2.26 μm

This strong line is not particularly sensitive to the IMF, being principally sensitive to the Ca abundance in the CvD16 models, with minor contributions from other elements. [Silva et al. \(2008\)](#) found that it did not correlate strongly with galaxy velocity dispersion, but showed significant scatter, whilst [Cesetti et al. \(2009\)](#) reported a loose positive correlation. Ca I 2.26 μm has not been well-studied using SSP modelling.

3.1.4 CO 2.30 μm bandhead

The extremely strong CO molecular absorption bands at the red end of the *K* band are most prominent in giant stars – and so decline in strength if the IMF is bottom heavy. A competing effect comes from [C/Fe], an increase in which will, of course, strengthen these features. The CO bandhead has in the past been used to measure stellar kinematics (e.g. [Lyubenova, Kuntschner & Silva 2008](#); [Vanderbeke et al. 2011](#)) as well finding use in discussions of stellar populations at an empirical level, e.g. [Silva et al. \(2008\)](#) and [Cesetti et al. \(2009\)](#). Both these studies found significant correlation between CO and measurements of optical features. [Davidge et al. \(2008\)](#) studied

radial variation in this feature’s strength in the central 1 arcsec of compact ellipticals, finding evidence for a complex radial behaviour in some galaxies; the strength rises out to $R = 0.3$ arcsec, then falls for $R > 0.3$ arcsec. [Mármol-Queraltó et al. \(2009\)](#) discussed the CO bandhead in the context of stellar population models, arguing that it could be used to test for extended star-formation histories in ETGs by probing the contribution to the light of intermediate-age stars.

3.2 Absorption feature gradients

In [Paper I](#), we were able to constrain the stellar population gradients in our sample, finding evidence for strong chemical abundance gradients that seemed to be fairly consistent across our sample. We now present radial gradients in the strengths of the *K*-band absorption lines we have measured (the first time these gradients have been measured, in some cases) and compare these with the predictions of the best-fitting model from [Paper I](#).

In [Fig. 2](#), we show the predictions derived from the models used in [Paper I](#) (i.e. the CvD12 models) against the new measurements, given the best-fitting parameters we found previously. These predictions indicate that the strength of the Ca features should be approximately constant with radius, which the data bear out. However, the ‘canonical’ model of [Paper I](#) severely overpredicts the strengths of the Ca I features. The canonical model used the minimum set of stellar population parameters required to explain the optical, IZ-, and YJ-band data adequately. That model also underpredicts the CO bandhead *a* line, but does not account for variations in the abundance of carbon, which the CO bandhead’s strength crucially depends on. In [Paper I](#), we explored a model with a [C/H] parameter included, finding this necessary to account for the low strength of the H β line. Whilst the value of this parameter was not very well constrained, this model is much less discrepant with the CO bandhead’s strength, suggesting good prospects for constraining the carbon abundance in the updated model framework. We also explored a model that incorporated two additional nuisance parameters, ΔT_{eff} and [O, Ne, S/ α]; this model produced much better estimates for the Ca I lines. Finally, the Na I 2.21 μm line exhibits a steeper gradient than is predicted in any of the models used in [Paper I](#) (despite the steep [Na/H] gradient we inferred).

The model sensitivities of these features and good S/N of some of our measurements indicate that these data will add significant additional constraining power to our stellar population analysis. In [Table 3](#), we give the best-fitting empirical spectroscopic gradients derived for these features (via the same procedure as in [Paper I](#)), with associated statistical uncertainties.

The strengths of the Na I 2.21 μm feature and the CO *a* line appear to flatten/turn over in the innermost region, where two spectra were extracted from the central Integral Field Unit (IFU) for each galaxy. It is important to understand whether this issue results from real variation of the stellar populations or some unaccounted-for observational effect. An instrumental issue seems unlikely, as the two data points are extracted from the same IFU. Furthermore, the effect is not seen in the Ca I 2.26 μm feature. The effects of observational seeing can, in principle, reduce the difference between the two measurements by spreading light from one region into another; we expect this effect to be limited since the seeing for these observations was typically < 1.4 arcsec (the central extraction region has this diameter). Nor is the seeing for these observations notably worse (on average) than for the IZ and YJ observations we made.

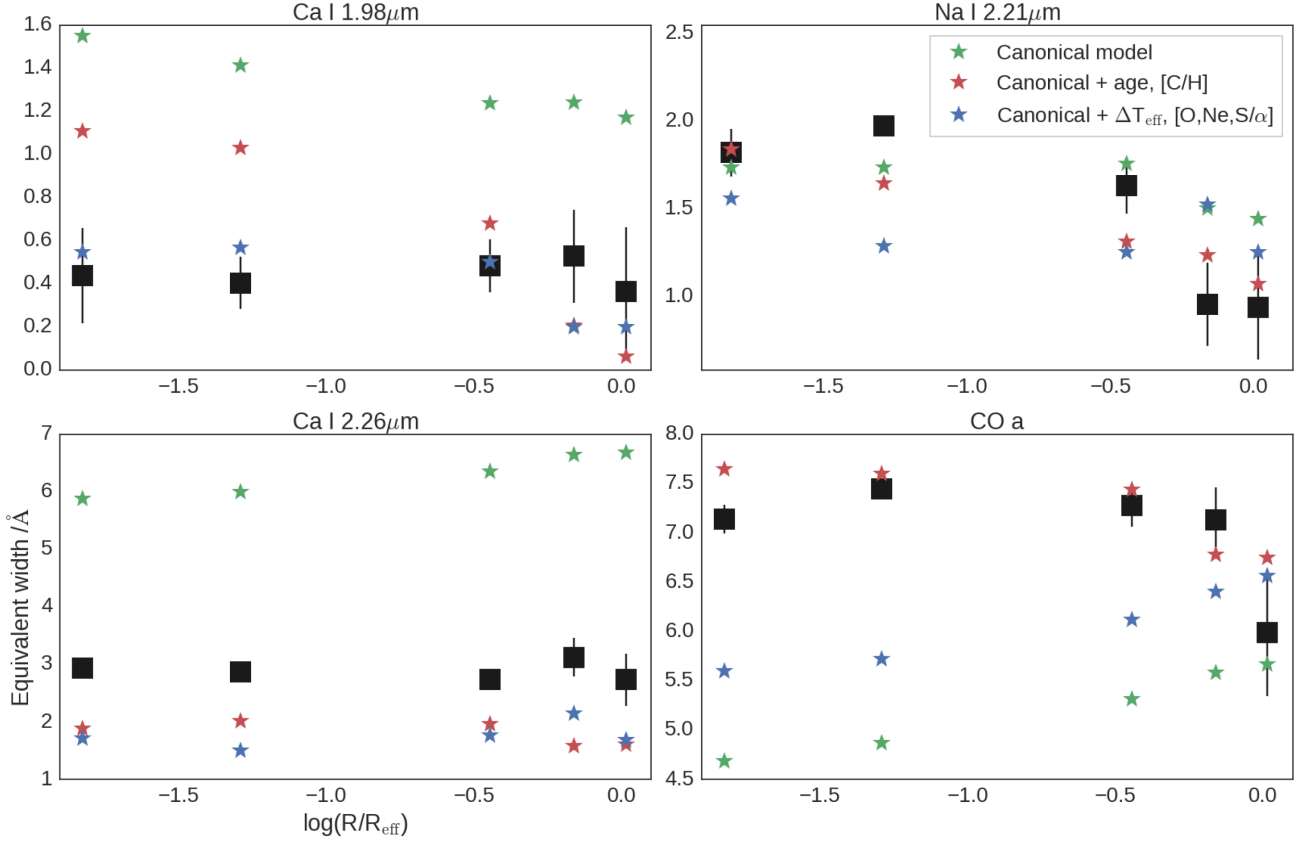


Figure 2. Measurements from the stacked KMOS *K*-band spectra with errors (large black symbols). Also shown are the predictions of the best-fitting models from Paper I, which were *not* constrained using these data (i.e. these are true predictions). *Green*: the ‘canonical model’ of Paper I (which accounts for $[\alpha/\text{H}]$, $[\text{Fe}/\text{H}]$, $[\text{Na}/\text{H}]$, $[\text{Ca}/\alpha]$, $[\text{K}/\text{H}]$, as well as the IMF). *Red*: an extended model which additionally accounts for stellar population age and $[\text{C}/\text{H}]$ (the inclusion of both proved necessary to fit the optical $\text{H}\beta$ line measurements taken from ATLAS^{3D}). *Blue*: an extended version of the canonical model with the fitting process marginalized over the nuisance parameters ΔT_{eff} and $[\text{O}, \text{Ne}, \text{S}/\alpha]$. This made little difference in the fits to the IZ & YJ band data.

Table 3. Best-fitting radial gradients (change in equivalent width per decade in radius) derived from the KMOS stacks.

Feature	Best-fitting gradient (\AA) per dex in $\log(R/R_{\text{eff}})$
Ca I 1.98 μm	0.05 ± 0.02
Na I 2.21 μm	-0.53 ± 0.08
Ca I 2.26 μm	-0.08 ± 0.09
CO 2.30 $\mu\text{m a}$	-0.11 ± 0.13

4 STELLAR POPULATION ANALYSIS

4.1 Updated model implementation

For this work, as in Paper I, model parameter estimation is accomplished using the EMCEE routine (Foreman-Mackey et al. 2013). This is a PYTHON implementation of an affine-invariant Markov chain Monte Carlo (MCMC) ensemble sampler (see Goodman & Weare 2010) used to characterize the posterior probability distribution for a chosen model, given data and statistical uncertainties.

For this purpose, we here make use of an updated version of the CvD12 models used in Paper I. The CvD16 models are constructed from an expanded library of stellar spectral templates incorporating stars with a variety of metallicities (Villaume et al. 2017), spanning the range $[\text{Z}/\text{H}] = -1.5$ to $[\text{Z}/\text{H}] = +0.2$. In Fig. 3, we show a few of these models corresponding to the *K*-band spectra of different

stellar populations with different chemical abundance patterns and IMFs.

The CvD16 models allow more freedom in the IMF parametrization. In Paper I, IMF variations were parametrized with a single parameter, f_{dwarf} , whilst the underlying shape of the IMF was assumed to be a single power-law below $1 M_{\odot}$. f_{dwarf} was defined as the fractional (*J*-band) luminosity contributed by stars of mass less than $0.5 M_{\odot}$.

In Paper I, we showed that for the spectral features used in our earlier analysis, index strength variations are approximately linear with respect to the f_{dwarf} parameter, with little dependence on the IMF shape. However, the models indicate that the effect of IMF shape is *not* negligible for the *K*-band indices we have measured here. This is because the strengths of different features trace the contribution to the light from stars in different mass ranges. Full details are given in Appendix B.

Because of this dependence on the IMF shape, in this work we use models with additional freedom in the IMF parametrization. Therefore, in this work the IMF is modelled as a broken power law, comprising two sections ($0.08\text{--}0.5 M_{\odot}$ and $0.5\text{--}1.0 M_{\odot}$) with independent power-law slopes $X1$ and $X2$. In this formalism, the Kroupa IMF (i.e. the Milky Way IMF) can be specified by $X1 = 1.3$, $X2 = 2.3$.

The CvD16 models also make use of a different approach to modelling the chemical abundance pattern of the stellar populations to the CvD12 models. The overall metallicity of the population is

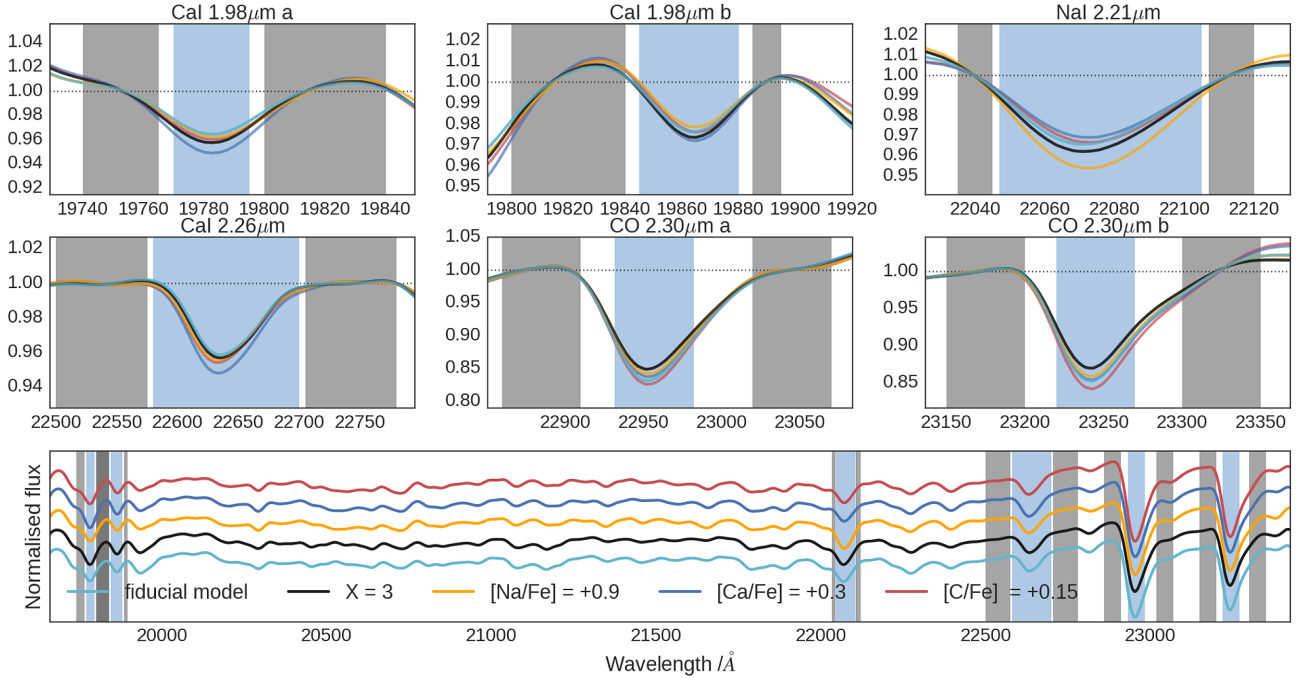


Figure 3. A subset of the CvD16 models used in this work broadened to a velocity dispersion of 230 km s^{-1} , indicating the effect of particularly important parameters. The fiducial model is for a 13.7 Gyr old population formed via a Kroupa IMF, with a solar abundance pattern. *Lower panel:* full models for the K band with measured feature bands indicated in blue and associated pseudo-continuum bands in grey. *Upper panels:* close-up view of each measured feature, with the models normalized with respect to the feature pseudo-continua.

Table 4. List of model parameters used in the MCMC inference. X1 and X2 are the IMF power-law slopes over the stellar mass intervals 0.08–0.5 and 0.5– $1.0 M_{\odot}$. Z is the total metallicity of the population and the $[X/Z]$ parameters are the relative variations of individual elements with respect to the overall metallicity.

Model parameter	Minimum value	Maximum value
$\log(t_{\text{age}}/\text{Gyr})$	$\log(7.0)$	$\log(14.0)$
X1	1.0	3.5
X2	1.0	3.5
$[Z/H]$	−1.0	0.4
$[Fe/Z]$	−0.5	0.3
$[Mg/Z]$	−0.4	0.6
$[Ca/Z]$	−0.4	0.4
$[Ti/Z]$	−0.4	0.6
[O, Ne, S/Z]	−0.3	0.3
$[Na/Z]$	−0.6	0.9
$[K/Z]$	−0.3	0.3
$[C/Z]$	−0.3	0.3

now represented using the relative logarithmic abundance $[Z/H]$ (where $[Z/H] = 0$ corresponds to the solar abundance pattern), whilst individual variations in element abundances are computed with respect to the overall metallicity (i.e. they are parametrized as $[X/Z]$). In addition, the response of the index strengths to variations in the abundance of particular elements varies with $[Z/H]$ in the updated models, meaning the responses are now coupled.

The full set of parameters used in this work for population inference is given in Table 4, along with the cut-off limits of the prior distribution.

For the purpose of presenting our results, some of the model parameters are remapped to alternative quantities for clarity and ease of comparison with other works. Stellar population age rather than

$\log(t_{\text{age}})$ is given. The segmented IMF slopes are converted to f_{dwarf} and also to the relative V -band M/L. The latter describes the ratio of M/L for two populations, one formed via the chosen IMF and the other according to a Kroupa IMF (but, to aid comparison, without adjusting for metallicity or age; we assume $[Z/H] = 0$ and $t_{\text{age}} = 13.5 \text{ Gyr}$). To describe the abundances, we compute $[Fe/H] = [Fe/Z] + [Z/H]$ and, for each of the other elements, $[X/Fe] = [X/Z] - [Fe/Z]$. These quantities are further adjusted to account for measured deviations in $[X/Fe]$ from the solar ratio in the library stars of different metallicities using the same recipe as was employed in van Dokkum et al. (2017).

4.2 Comparison with previous model implementation

To allow a meaningful comparison, we first use these models to fit the optical, IZ -, and YJ -band stacked data presented in Paper I in order to (a) reproduce the results already given and (b) highlight any differences due to the model changes prior to including the information from our new K -band measurements, i.e. isolate the effect of updating the model framework.

To achieve this, we set up the models with the constraint $X1 = X2$ (i.e. we limited ourselves to the case of a single power-law description of the IMF). We assumed an old age ($t = 13.5 \text{ Gyr}$) and included measurements of the optical features Fe 5015 and Mgb in the fit. We fit for metallicity, the IMF slope, and abundance variations in Fe, Mg, Na, Ca, and K. The results of a set of MCMC runs with 100 walkers and 900 steps (after 100 burn-in steps) are given in Table 5.

These results are broadly consistent with those presented in Paper I (table 9). For clarity, we reorganize those results so that they are reported in terms of the same parameters as in Table 5 and can thus be directly compared (see Table 6). We detect a very

Table 5. Estimated parameter values for the stacked spectra first presented in [Paper I](#), acquired using the CvD16 models. We set $X1 = X2 = X$ and fit for $[Z/H]$ as well as the abundances of various elements of interest. R1 and R2 correspond to the two extraction regions in the central IFU (<0.7 arcsec, >0.7 arcsec), whilst R3, R4, and R5 correspond to the rings of IFUs arranged at $\sim 1/3 R_{\text{eff}}$, $\sim 2/3 R_{\text{eff}}$, and $\sim R_{\text{eff}}$.

	R1	R2	R3	R4	R5	Gradient
X	$1.07^{+0.50}_{-0.05}$	$1.07^{+0.51}_{-0.05}$	$2.16^{+0.55}_{-0.74}$	$1.22^{+1.07}_{-0.14}$	$2.71^{+0.53}_{-1.10}$	0.49 ± 0.36
$[Z/H]$	$0.24^{+0.04}_{-0.05}$	$0.14^{+0.03}_{-0.04}$	$-0.03^{+0.06}_{-0.11}$	$-0.07^{+0.09}_{-0.13}$	$-0.15^{+0.13}_{-0.15}$	-0.22 ± 0.05
$[\text{Fe}/\text{H}]$	$-0.07^{+0.07}_{-0.06}$	$-0.19^{+0.05}_{-0.07}$	$-0.26^{+0.08}_{-0.12}$	$-0.31^{+0.12}_{-0.13}$	$-0.25^{+0.14}_{-0.18}$	-0.13 ± 0.04
$[\text{Mg}/\text{Fe}]$	$0.41^{+0.06}_{-0.05}$	$0.44^{+0.05}_{-0.05}$	$0.40^{+0.09}_{-0.07}$	$0.43^{+0.10}_{-0.12}$	$0.28^{+0.15}_{-0.14}$	-0.03 ± 0.03
$[\text{Na}/\text{Fe}]$	$0.84^{+0.09}_{-0.09}$	$0.73^{+0.06}_{-0.07}$	$0.43^{+0.15}_{-0.27}$	$0.35^{+0.27}_{-0.38}$	$-0.12^{+0.47}_{-0.31}$	-0.38 ± 0.13
$[\text{Ca}/\text{Fe}]$	$0.17^{+0.08}_{-0.08}$	$0.16^{+0.07}_{-0.06}$	$0.11^{+0.10}_{-0.10}$	$0.04^{+0.14}_{-0.14}$	$-0.01^{+0.15}_{-0.21}$	-0.08 ± 0.04
$[\text{K}/\text{Fe}]$	$0.16^{+0.12}_{-0.14}$	$0.11^{+0.11}_{-0.10}$	$0.06^{+0.23}_{-0.18}$	$0.16^{+0.22}_{-0.23}$	$0.19^{+0.27}_{-0.30}$	-0.00 ± 0.08
f_{dwarf} (per cent)	$2.2^{+1.5}_{-0.2}$	$2.2^{+1.6}_{-0.1}$	$2.9^{+7.0}_{-0.6}$	$2.8^{+6.0}_{-0.5}$	$3.2^{+13.0}_{-0.9}$	0.3 ± 2.7
M/L	$0.70^{+0.18}_{-0.02}$	$0.69^{+0.18}_{-0.02}$	$0.79^{+0.96}_{-0.08}$	$0.78^{+0.82}_{-0.08}$	$0.86^{+2.04}_{-0.13}$	0.04 ± 0.35

Table 6. The results presented in [Paper I](#) with the parameters reorganized to match those presented in Table 5.

	R1	R2	R3	R4	R5	Gradient
$[\text{Fe}/\text{H}]$	$0.06^{+0.03}_{-0.03}$	$-0.06^{+0.03}_{-0.03}$	$-0.21^{+0.05}_{-0.05}$	$-0.21^{+0.08}_{-0.08}$	$-0.21^{+0.10}_{-0.10}$	-0.17 ± 0.02
$[\alpha/\text{Fe}]$	$0.34^{+0.04}_{-0.04}$	$0.34^{+0.04}_{-0.04}$	$0.33^{+0.06}_{-0.06}$	$0.31^{+0.09}_{-0.09}$	$0.21^{+0.12}_{-0.12}$	-0.03 ± 0.02
$[\text{Na}/\text{Fe}]$	$0.62^{+0.12}_{-0.12}$	$0.53^{+0.08}_{-0.08}$	$0.21^{+0.16}_{-0.19}$	$0.21^{+0.25}_{-0.35}$	$-0.15^{+0.45}_{-0.50}$	-0.31 ± 0.07
$[\text{Ca}/\text{Fe}]$	$-0.02^{+0.06}_{-0.06}$	$0.00^{+0.06}_{-0.06}$	$0.02^{+0.08}_{-0.08}$	$-0.10^{+0.13}_{-0.13}$	$-0.22^{+0.18}_{-0.08}$	-0.03 ± 0.02
f_{dwarf} (per cent)	$9.4^{+2.1}_{-2.1}$	$11.1^{+1.5}_{-1.5}$	$10.5^{+2.1}_{-2.2}$	$6.7^{+3.9}_{-1.6}$	$8.0^{+5.6}_{-2.5}$	-0.6 ± 0.8

similar gradient in $[\text{Fe}/\text{H}]$ and find $[\text{Mg}/\text{Fe}]$ strongly enhanced and constant with radius. We also now explicitly calculate the $[Z/H]$ gradient: previously, it was implicitly assumed that $[Z/H] = 0$ at all radii. However, applying the empirical relationship $[Z/H] = [\text{Fe}/\text{H}] + 0.94[\alpha/\text{Fe}]$ set out in Thomas et al. (2003) would indicate a gradient of -0.20 ± 0.03 , consistent with the new result. Meanwhile $[\text{Ca}/\text{Fe}]$ is constant with radius, and it's clear that Ca is much less overabundant than Mg; the new model does however prefer a modest enhancement in the core, which was not the case previously. For $[\text{Na}/\text{Fe}]$, we infer a stronger enhancement than in [Paper I](#), although the two results are not strongly in tension and we find a consistent gradient. Finally, the IMF we infer is more Milky Way like, rather than modestly bottom heavy as found previously. In summary, using the updated models we find qualitatively similar results to those which were presented in [Paper I](#).

These results are more readily compared with the literature than in the form presented in [Paper I](#). It is instructive to make a comparison with the results of McDermid et al. (2015), which were calculated via the models of Schiavon (2007) using the same optical data we used for our analysis (and assuming no IMF variations). In the central $0.125 R_{\text{eff}}$ of the galaxies from our sample (excluding NGC 1407, which they did not observe) the median age they find is 13.7 ± 2.1 Gyr, the median $[Z/H] = 0.06 \pm 0.05$, and the median $[\alpha/\text{Fe}]$ is 0.28 ± 0.05 . The latter is a little lower than our value, which may be due to the different models used, the extra indices we fit, the use of additional parameters we include, or a combination of all of these.

In the next section, we present the results of our full analysis, making use of the K -band data as well as the optical/IZ/YJ measurements, additional stellar population parameters, and the data from individual galaxies.

5 RESULTS

We now use the CvD16 models in conjunction with all available data, including the KMOS measurements of the K -band indices, to infer stellar population parameters for our sample. As well as the data used in Section 4, we make use of the K -band data and include $H\beta$ in the fit: in [Paper I](#), we showed that $H\beta$'s sensitivity to various poorly constrained parameters such as $[\text{C}/\text{H}]$ and stellar age reduced its constraining power substantially. However, with the additional sensitivity to these parameters provided by the CO bandhead, our ability to constrain these parameters improves somewhat, unlocking $H\beta$'s potential as a constraint on the age of the stellar population.

Whilst we do not expect to be able to constrain the abundance of α elements other than Mg and Ca, we nevertheless marginalize over the parameters $[\text{Ti}/\text{Fe}]$ and $[\text{O}, \text{Ne}, \text{S}/\text{Fe}]$.

To obtain these results, we made use of all available feature measurements, with two exceptions. First, we found that in the updated model framework the predicted $\text{MgI } 0.88 \mu\text{m}$ line is much stronger, given the same stellar population parameter values. This puts the new model prediction in tension with the data (we show the change to the models in Fig. 4). Secondly, we were concerned that the CO $2.30 \mu\text{m } b$ line might be subject to much greater contamination (from a combination of increasing thermal background, stronger telluric absorption, and sky emission lines) than the CO $2.30 \mu\text{m } a$ line, although in the models the strengths of the two are strongly coupled. We therefore used only the a line in the fit. For this strong feature, the formal statistical uncertainty of the equivalent width is small, so we lose very little constraining power by doing this.

In Table 7, we give the best-fitting stellar population parameters inferred from the stacked spectra and provide best-fitting parameter gradients with associated statistical uncertainty. All MCMC runs used 100 walkers and 900 steps after a 100 step burn-in.

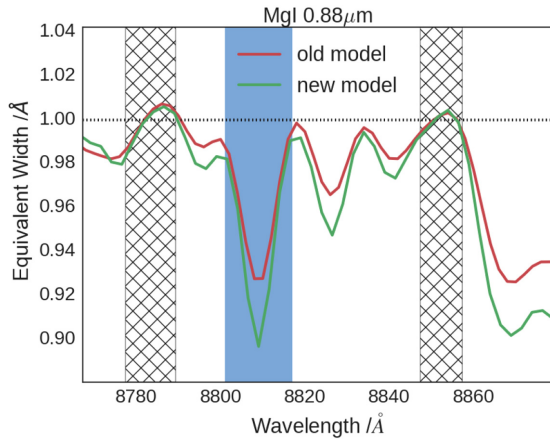


Figure 4. We show a fiducial case for the old (CvD12) and new (CvD16) SSP model grids, with a Kroupa IMF, solar abundance pattern, and a stellar population age of 13.5 Gyr. In the updated model grids (which we remind the reader are constructed from an expanded empirical spectral library), the Mg I 0.88 μm feature (the region around which we show here alongside feature and pseudo-continuum definitions) is much stronger.

5.1 Comparison with results from Paper I

Including the K -band measurements and additional model parameters modifies our results to some extent. In Fig. 5, we show the parameter values inferred from the stacks using only a limited set of indices (Mgb, Fe 5015, IZ - and YJ -band measurements) and model parameters (blue), and those inferred when data from the K band and $H\beta$ are included along with a comprehensive set of model parameters (red). Generally, as expected, our results are not radically altered with respect to those obtained previously, although the best-fitting $[Z/H]$ is an exception. The inferred IMF is consistent with Milky Way-like throughout. The inferred age is consistent being constant with radius (approximately 10 Gyr) or else gradually declining with radius. Whilst we initially as-

sumed an extremely old stellar population, this slight difference does not in practice affect the inferred values of the other model parameters.

In Fig. 6, we compare the two sets of model predictions to the actual measured line indices. This demonstrates several key points. For the most part, the simpler model reproduces the optical, IZ band, and YJ band indices adequately. However, as in Paper I, it is challenging to simultaneously fit NaI 0.82 μm and NaI 1.14 μm . By contrast, the updated model now underpredicts the strength of $H\beta$, whereas previously the model tended to overpredict $H\beta$. As noted in Paper I, increased abundance of carbon can weaken $H\beta$. The inclusion of a metallicity parameter in the model means we now implicitly assume $[C/H]$ rises in the core along with the α -elements and Fe, explaining this change. Likewise, whilst the CvD16 model grids do not include variations in $[Al/Fe]$, the AlI 1.31 μm feature's strength is no longer in strong tension with the model, suggesting that the assumption that aluminium tracks overall metallicity is reasonable. This is a significant advantage of the new model formalism.

However, the simpler model does a poor job of predicting the K -band indices (we remind the reader that the simpler model was not fit to these indices). This shows that the K -band indices are adding useful information, which we take advantage of by using the more sophisticated model with additional parameters (a two-part power-law IMF, stellar population age, $[C/Fe]$, $[Ti/Fe]$, and $[O, Ne, S/Fe]$). This model does a much better, though still imperfect job of fitting the K -band data, without compromising the fit to the bluer spectral features.

In Fig. 7, we show how the CvD16 spectral models corresponding to these parameters appear when directly compared to the data. Specifically, we show the spectral region around each index for the centrally extracted stack, normalized by the pseudo-continuum bands on either side of each feature. We thus view the stacked spectrum, as it appears when the index measurements are made. We remind the reader that the shaded regions of uncertainty correspond to the scatter amongst the spectra used to construct the stack, rather than the formal statistical error. We constructed the overplotted spectral models by linear interpolation of the CvD16 models,

Table 7. Headline results: estimated parameter values for the stacked spectra, acquired using the CvD16 models and the full set of index measurements. For the IMF, we fit a two-part power law with slopes X1 and X2, and we fit for stellar population age and total metallicity, as well as the abundances of various elements of interest. R1 and R2 correspond to the two extraction regions in the central IFU (<0.7 arcsec, >0.7 arcsec), whilst R3, R4, and R5 correspond to the rings of IFUs arranged at $\sim 1/3 R_{\text{eff}}$, $\sim 2/3 R_{\text{eff}}$, and $\sim R_{\text{eff}}$.

	R1	R2	R3	R4	R5	Gradient
Age /Gyr	$11.3^{+1.4}_{-1.3}$	$9.1^{+1.0}_{-0.7}$	$7.8^{+2.2}_{-0.5}$	$7.3^{+3.3}_{-0.2}$	$8.9^{+2.5}_{-1.2}$	-1.8 ± 0.8
X1	$2.01^{+0.51}_{-0.67}$	$1.10^{+0.67}_{-0.07}$	$1.12^{+0.86}_{-0.08}$	$1.98^{+0.66}_{-0.65}$	$2.86^{+0.41}_{-1.09}$	0.26 ± 0.39
X2	$1.24^{+0.90}_{-0.16}$	$1.06^{+0.43}_{-0.05}$	$1.49^{+0.87}_{-0.32}$	$1.52^{+0.96}_{-0.35}$	$1.82^{+1.02}_{-0.53}$	0.31 ± 0.40
$[Z/H]$	$0.17^{+0.03}_{-0.04}$	$0.23^{+0.02}_{-0.02}$	$0.14^{+0.04}_{-0.05}$	$0.02^{+0.07}_{-0.11}$	$-0.14^{+0.13}_{-0.11}$	-0.11 ± 0.03
$[Fe/H]$	$-0.12^{+0.07}_{-0.11}$	$-0.08^{+0.05}_{-0.06}$	$-0.26^{+0.14}_{-0.07}$	$-0.33^{+0.15}_{-0.13}$	$-0.30^{+0.20}_{-0.18}$	-0.16 ± 0.05
$[Mg/Fe]$	$0.48^{+0.10}_{-0.05}$	$0.44^{+0.05}_{-0.05}$	$0.42^{+0.08}_{-0.10}$	$0.51^{+0.12}_{-0.14}$	$0.38^{+0.17}_{-0.17}$	-0.01 ± 0.04
$[Na/Fe]$	$0.77^{+0.12}_{-0.10}$	$0.70^{+0.06}_{-0.05}$	$0.43^{+0.13}_{-0.16}$	$0.34^{+0.21}_{-0.35}$	$-0.11^{+0.40}_{-0.31}$	-0.35 ± 0.09
$[Ca/Fe]$	$0.20^{+0.11}_{-0.07}$	$0.09^{+0.06}_{-0.05}$	$0.09^{+0.11}_{-0.09}$	$0.11^{+0.17}_{-0.14}$	$0.08^{+0.16}_{-0.25}$	-0.04 ± 0.05
$[O, Ne, S/Fe]$	$0.78^{+0.13}_{-0.19}$	$0.64^{+0.09}_{-0.10}$	$0.73^{+0.14}_{-0.15}$	$0.70^{+0.19}_{-0.23}$	$0.73^{+0.19}_{-0.40}$	0.02 ± 0.06
$[Ti/Fe]$	$0.53^{+0.18}_{-0.16}$	$0.22^{+0.12}_{-0.10}$	$0.18^{+0.19}_{-0.25}$	$0.57^{+0.23}_{-0.33}$	$0.39^{+0.31}_{-0.46}$	-0.05 ± 0.11
$[C/Fe]$	$0.11^{+0.10}_{-0.14}$	$0.07^{+0.05}_{-0.08}$	$0.15^{+0.12}_{-0.13}$	$0.22^{+0.16}_{-0.18}$	$0.09^{+0.24}_{-0.20}$	0.06 ± 0.04
$[K/Fe]$	$0.19^{+0.17}_{-0.13}$	$0.07^{+0.11}_{-0.06}$	$0.19^{+0.15}_{-0.16}$	$0.25^{+0.21}_{-0.20}$	$0.17^{+0.29}_{-0.29}$	0.06 ± 0.05
f_{dwarf} (per cent)	$3.9^{+2.8}_{-0.9}$	$2.7^{+1.3}_{-0.4}$	$4.9^{+2.0}_{-1.5}$	$5.7^{+3.0}_{-2.0}$	$6.5^{+5.7}_{-2.2}$	2.0 ± 1.7
M/L	$0.91^{+0.37}_{-0.12}$	$0.75^{+0.16}_{-0.05}$	$0.95^{+0.28}_{-0.14}$	$1.04^{+0.45}_{-0.21}$	$1.32^{+0.85}_{-0.35}$	0.19 ± 0.13

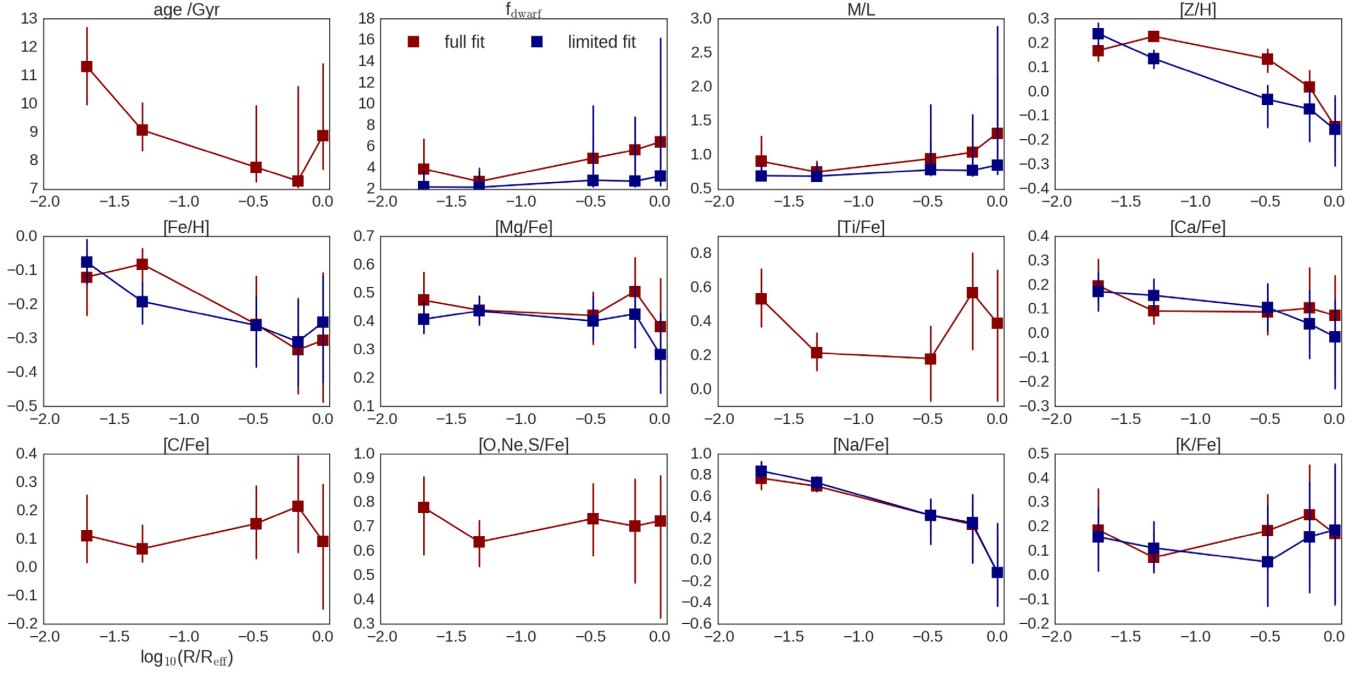


Figure 5. Parameter radial variations via two model fits. The parameters inferred from the stacked spectra using only a limited set of indices and a restricted parameter set are shown in blue, whilst those inferred when data from the *K* band and $H\beta$ and additional model parameters are included are shown in red. Generally, as expected, our results are not radically altered with respect to those obtained previously, although the best-fitting $[Z/H]$ is an exception.

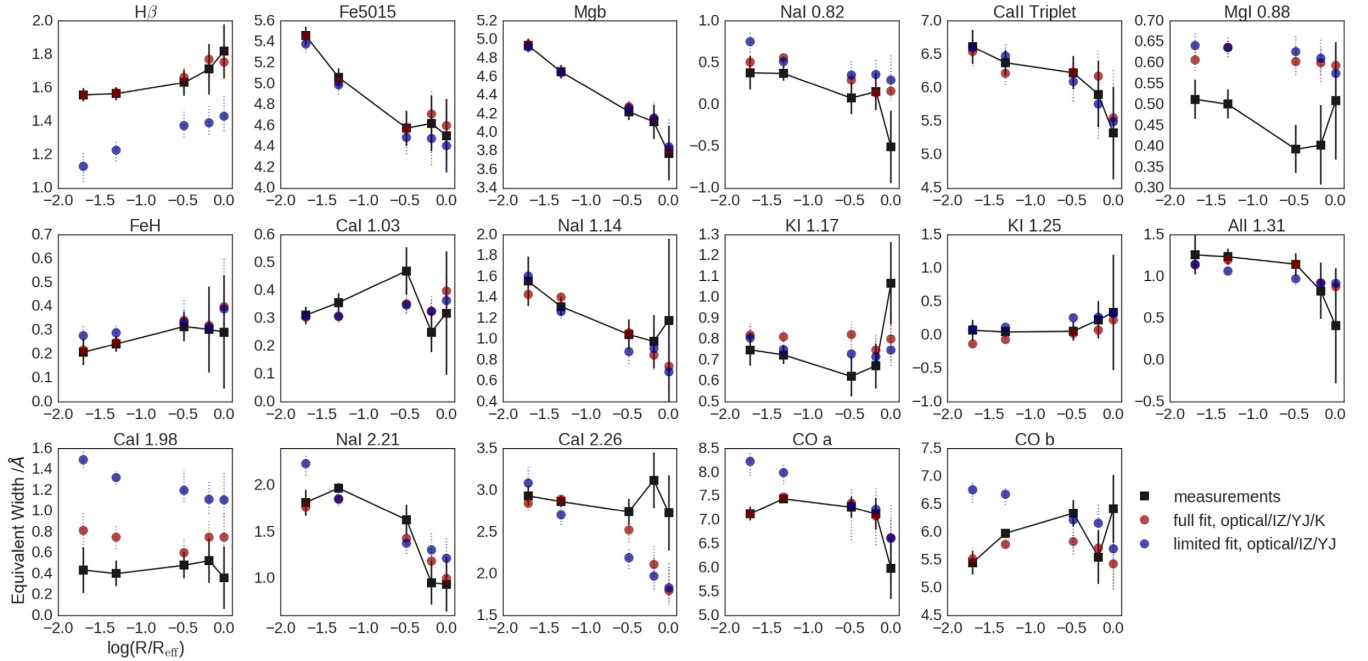


Figure 6. Two sets of model predictions (equivalent widths in Å) generated from the parameters shown in Fig. 5. The simpler model (blue) was not fit to $H\beta$, MgI 0.88 μm , AlI 1.31 μm , or any of the *K*-band indices. The more complex model uses more parameters and is fit to $H\beta$ and the *K*-band features (except CO *b*). As with the simpler model, it is not fit to MgI 0.88 μm or AlI 1.31 μm .

broadening this model to the velocity dispersion found using pPXF. We can thereby closely examine those features where the measured index strength is less well fit by the model and perhaps determine the cause.

5.2 Results for individual galaxies

In this section, we report the results for individual galaxies, comparing these with the average radial trends obtained from the stacked data. We fit these galaxies with the same set of model param-

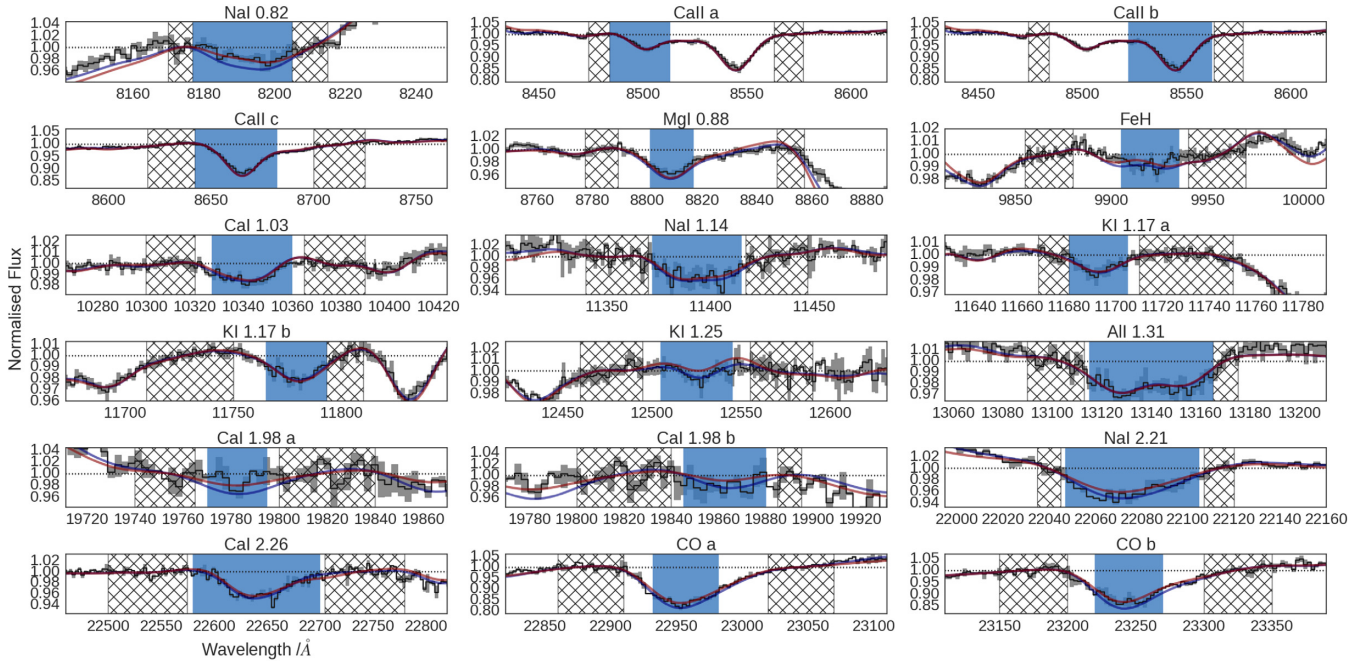


Figure 7. The centrally extracted stacked spectrum in the region of each index definition with shaded uncertainties, alongside models generated from the parameters shown in Fig. 5 (same colour scheme). The feature band for each index is shaded blue, whilst the pseudo-continuum regions are hatched. Although the model parameters are inferred from the measured equivalent widths, in most cases the models match the data within the uncertainties fairly well, especially for the strongest features. Note that spectra are normalized with respect to the pseudo-continuum (e.g. Na I 0.82 μm looks quite different to its appearance in the ‘raw’ spectra because of this).

Table 8. Estimated parameter values for the spectra extracted at $\sim 0.02 R_{\text{eff}}$, acquired using the updated models and the full set of index measurements. We fit for population age, a two-part power-law IMF, and $[Z/H]$, as well as the abundances of various elements of interest. Note that we did not obtain additional K-band data for NGC 0524, but have none the less fit the data via the updated model formalism.

	NGC 0524	NGC 1407	NGC 3377	NGC 3379	NGC 4552	NGC 4621	NGC 5813
Age /Gyr	$10.2^{+2.40}_{-1.96}$	$7.36^{+2.85}_{-0.25}$	$7.08^{+0.58}_{-0.06}$	$7.11^{+0.89}_{-0.07}$	$7.09^{+0.62}_{-0.06}$	$12.69^{+0.87}_{-2.33}$	$8.04^{+2.24}_{-0.73}$
X1	$2.06^{+0.73}_{-0.70}$	$1.83^{+0.59}_{-0.54}$	$2.68^{+0.38}_{-1.02}$	$1.10^{+0.89}_{-0.07}$	$2.47^{+0.55}_{-0.92}$	$1.24^{+0.66}_{-0.16}$	$1.56^{+0.71}_{-0.38}$
X2	$1.46^{+1.10}_{-0.29}$	$1.16^{+1.31}_{-0.11}$	$1.10^{+0.74}_{-0.07}$	$1.22^{+0.44}_{-0.15}$	$1.16^{+1.14}_{-0.11}$	$1.08^{+0.53}_{-0.05}$	$2.04^{+0.87}_{-0.66}$
$[Z/H]$	$0.09^{+0.06}_{-0.08}$	$0.17^{+0.10}_{-0.17}$	$0.15^{+0.04}_{-0.04}$	$0.24^{+0.06}_{-0.05}$	$0.28^{+0.04}_{-0.05}$	$0.22^{+0.05}_{-0.05}$	$0.13^{+0.06}_{-0.05}$
$[Fe/H]$	$0.04^{+0.09}_{-0.17}$	$-0.21^{+0.17}_{-0.13}$	$-0.07^{+0.08}_{-0.11}$	$-0.17^{+0.06}_{-0.06}$	$0.24^{+0.05}_{-0.10}$	$0.13^{+0.06}_{-0.06}$	$-0.18^{+0.11}_{-0.10}$
$[Mg/Fe]$	$0.38^{+0.12}_{-0.08}$	$0.79^{+0.14}_{-0.34}$	$0.34^{+0.10}_{-0.05}$	$0.55^{+0.06}_{-0.05}$	$0.40^{+0.06}_{-0.07}$	$0.25^{+0.06}_{-0.06}$	$0.60^{+0.09}_{-0.09}$
$[Na/Fe]$	$0.35^{+0.09}_{-0.09}$	$0.71^{+0.15}_{-0.30}$	$0.62^{+0.08}_{-0.08}$	$0.73^{+0.07}_{-0.09}$	$0.90^{+0.06}_{-0.06}$	$0.82^{+0.05}_{-0.05}$	$0.59^{+0.11}_{-0.10}$
$[Ca/Fe]$	$0.13^{+0.14}_{-0.07}$	$0.36^{+0.15}_{-0.12}$	$0.01^{+0.09}_{-0.06}$	$0.26^{+0.05}_{-0.06}$	$0.04^{+0.08}_{-0.05}$	$0.12^{+0.04}_{-0.06}$	$0.29^{+0.08}_{-0.10}$
	$-0.24^{+0.22}_{-0.19}$	$-0.05^{+0.63}_{-0.19}$	$0.55^{+0.16}_{-0.12}$	$0.89^{+0.10}_{-0.17}$	$-0.13^{+0.16}_{-0.22}$	$0.61^{+0.07}_{-0.09}$	$0.53^{+0.22}_{-0.20}$
$[O, Ne, S/Fe]$							
$[Ti/Fe]$	$0.39^{+0.24}_{-0.18}$	$0.84^{+0.13}_{-0.43}$	$0.40^{+0.19}_{-0.14}$	$0.64^{+0.12}_{-0.11}$	$0.23^{+0.15}_{-0.14}$	$-0.23^{+0.13}_{-0.09}$	$0.71^{+0.16}_{-0.20}$
$[C/Fe]$	$0.16^{+0.15}_{-0.22}$	$0.20^{+0.18}_{-0.15}$	$0.36^{+0.12}_{-0.08}$	$0.61^{+0.06}_{-0.06}$	$0.16^{+0.08}_{-0.10}$	$0.12^{+0.08}_{-0.09}$	$0.14^{+0.15}_{-0.12}$
$[K/Fe]$	$0.17^{+0.17}_{-0.19}$	$0.55^{+0.11}_{-0.35}$	$0.15^{+0.16}_{-0.15}$	$0.36^{+0.22}_{-0.15}$	$-0.05^{+0.18}_{-0.13}$	$0.09^{+0.13}_{-0.16}$	$0.13^{+0.23}_{-0.12}$
f_{dwarf} (per cent)	$4.83^{+4.97}_{-1.60}$	$4.41^{+3.60}_{-1.06}$	$4.92^{+2.87}_{-1.57}$	$3.12^{+1.53}_{-0.56}$	$6.61^{+3.11}_{-2.32}$	$3.06^{+1.29}_{-0.55}$	$5.71^{+2.81}_{-1.74}$
M/L	$1.04^{+0.71}_{-0.22}$	$1.00^{+0.45}_{-0.15}$	$1.00^{+0.48}_{-0.18}$	$0.80^{+0.21}_{-0.07}$	$1.08^{+0.58}_{-0.21}$	$0.79^{+0.17}_{-0.06}$	$1.11^{+0.34}_{-0.21}$

ters and features as the stack where possible, although for some galaxies a full set of features is not available (note that we do not provide fits for NGC 4486 since, as noted in Paper I, the optical data suffer from contamination by AGN emission). Results are provided for the three innermost extraction regions (the subdivided central IFU field and the innermost ring of IFUs at

$\sim \frac{1}{3} R_{\text{eff}}$) where the S/N is sufficient. For each extraction region, we present a table of results spanning the full sample (see Tables 8–10). Note that we did not obtain additional K-band data for NGC 0524 but have none the less fit the data via the updated model formalism. Likewise, we have created fits for NGC 1407 and NGC 3379 for which YJ-band data were not available.

Table 9. Estimated parameter values for the spectra extracted at $\sim 0.05 R_{\text{eff}}$, acquired using the updated models and the full set of index measurements. We fit for population age, a two-part power-law IMF, and [Z/H], as well as the abundances of various elements of interest. Note that we did not obtain additional K-band data for NGC 0524 but have none the less fit the data via the updated model formalism.

	NGC 0524	NGC 1407	NGC 3377	NGC 3379	NGC 4552	NGC 4621	NGC 5813
age /Gyr	$13.54^{+0.32}_{-3.72}$	$8.92^{+2.84}_{-1.32}$	$7.16^{+1.12}_{-0.11}$	$7.26^{+1.90}_{-0.19}$	$7.09^{+0.54}_{-0.06}$	$10.61^{+1.74}_{-2.04}$	$7.48^{+3.70}_{-0.33}$
X1	$2.27^{+0.53}_{-0.77}$	$1.50^{+1.06}_{-0.33}$	$2.45^{+0.58}_{-0.64}$	$1.10^{+1.01}_{-0.07}$	$3.36^{+0.10}_{-1.09}$	$1.20^{+0.84}_{-0.14}$	$1.88^{+0.67}_{-0.57}$
X2	$1.14^{+1.43}_{-0.09}$	$2.08^{+0.79}_{-0.69}$	$1.09^{+0.49}_{-0.06}$	$1.10^{+0.63}_{-0.07}$	$2.14^{+0.62}_{-0.60}$	$1.11^{+0.97}_{-0.08}$	$3.29^{+0.14}_{-1.63}$
[Z/H]	$-0.01^{+0.06}_{-0.12}$	$-0.21^{+0.26}_{-0.16}$	$0.01^{+0.04}_{-0.05}$	$0.11^{+0.07}_{-0.06}$	$0.23^{+0.05}_{-0.05}$	$0.17^{+0.06}_{-0.05}$	$0.08^{+0.08}_{-0.08}$
[Fe/H]	$-0.13^{+0.09}_{-0.13}$	$-0.32^{+0.18}_{-0.24}$	$-0.43^{+0.10}_{-0.07}$	$-0.26^{+0.07}_{-0.08}$	$-0.05^{+0.09}_{-0.10}$	$0.02^{+0.06}_{-0.09}$	$-0.12^{+0.10}_{-0.16}$
[Mg/Fe]	$0.42^{+0.12}_{-0.08}$	$0.49^{+0.28}_{-0.36}$	$0.51^{+0.08}_{-0.09}$	$0.63^{+0.05}_{-0.08}$	$0.53^{+0.10}_{-0.07}$	$0.35^{+0.07}_{-0.06}$	$0.47^{+0.13}_{-0.08}$
[Na/Fe]	$0.22^{+0.12}_{-0.11}$	$0.77^{+0.15}_{-0.26}$	$0.79^{+0.07}_{-0.12}$	$0.71^{+0.07}_{-0.13}$	$0.89^{+0.08}_{-0.06}$	$0.72^{+0.08}_{-0.05}$	$0.53^{+0.11}_{-0.09}$
[Ca/Fe]	$0.15^{+0.12}_{-0.06}$	$0.45^{+0.15}_{-0.17}$	$0.38^{+0.06}_{-0.09}$	$0.27^{+0.05}_{-0.08}$	$0.18^{+0.10}_{-0.07}$	$0.18^{+0.06}_{-0.05}$	$0.21^{+0.14}_{-0.06}$
[O, Ne, S/Fe]	$0.31^{+0.22}_{-0.25}$	$0.43^{+0.30}_{-0.43}$	$0.69^{+0.19}_{-0.15}$	$0.80^{+0.14}_{-0.31}$	$0.10^{+0.14}_{-0.23}$	$0.68^{+0.09}_{-0.11}$	$0.41^{+0.25}_{-0.19}$
[Ti/Fe]	$0.33^{+0.24}_{-0.25}$	$0.35^{+0.39}_{-0.33}$	$0.79^{+0.18}_{-0.20}$	$0.71^{+0.14}_{-0.15}$	$0.64^{+0.16}_{-0.15}$	$-0.11^{+0.17}_{-0.10}$	$0.31^{+0.31}_{-0.18}$
[C/Fe]	$0.20^{+0.14}_{-0.23}$	$0.16^{+0.28}_{-0.16}$	$0.50^{+0.11}_{-0.11}$	$0.58^{+0.08}_{-0.10}$	$0.36^{+0.09}_{-0.14}$	$0.24^{+0.09}_{-0.11}$	$0.14^{+0.16}_{-0.15}$
[K/Fe]	$0.15^{+0.16}_{-0.17}$	$0.25^{+0.25}_{-0.26}$	$0.67^{+0.06}_{-0.17}$	$0.44^{+0.16}_{-0.22}$	$0.26^{+0.14}_{-0.15}$	$0.09^{+0.12}_{-0.13}$	$-0.05^{+0.16}_{-0.08}$
f_{dwarf} (per cent)	$6.58^{+3.72}_{-2.34}$	$5.23^{+4.32}_{-1.63}$	$4.89^{+2.59}_{-1.36}$	$3.90^{+1.62}_{-1.09}$	$10.66^{+3.04}_{-3.16}$	$4.14^{+1.93}_{-1.06}$	$4.35^{+5.04}_{-1.13}$
M/L	$1.31^{+0.50}_{-0.35}$	$1.07^{+0.60}_{-0.21}$	$1.04^{+0.44}_{-0.19}$	$0.89^{+0.24}_{-0.13}$	$1.93^{+0.55}_{-0.55}$	$0.94^{+0.24}_{-0.14}$	$0.93^{+0.66}_{-0.13}$

Table 10. Estimated parameter values for the spectra extracted at $\sim \frac{1}{3} R_{\text{eff}}$, acquired using the updated models and the full set of index measurements. We fit for population age, a two-part power-law IMF, and [Z/H], as well as the abundances of various elements of interest. Note that we did not obtain additional K-band data for NGC 0524 but have none the less fit the data via the updated model formalism.

	NGC 0524	NGC 1407	NGC 3377	NGC 3379	NGC 4552	NGC 4621	NGC 5813
Age /Gyr	$11.18^{+1.80}_{-2.54}$	$7.45^{+3.34}_{-0.29}$	$9.14^{+2.86}_{-1.44}$	$8.89^{+1.98}_{-1.22}$	$8.56^{+3.23}_{-0.99}$	$10.04^{+2.29}_{-1.84}$	$9.69^{+2.93}_{-1.74}$
X1	$2.37^{+0.67}_{-0.88}$	$1.66^{+0.80}_{-0.45}$	$1.73^{+0.88}_{-0.48}$	$2.12^{+0.63}_{-0.76}$	$2.50^{+0.59}_{-0.89}$	$1.86^{+0.81}_{-0.57}$	$3.05^{+0.28}_{-1.23}$
X2	$2.61^{+0.55}_{-1.07}$	$1.12^{+1.10}_{-0.08}$	$1.26^{+1.19}_{-0.17}$	$2.10^{+0.81}_{-0.68}$	$3.30^{+0.13}_{-1.40}$	$1.31^{+0.96}_{-0.21}$	$1.22^{+1.36}_{-0.15}$
[Z/H]	$-0.08^{+0.11}_{-0.14}$	$0.36^{+0.03}_{-0.25}$	$-0.43^{+0.14}_{-0.27}$	$0.03^{+0.10}_{-0.09}$	$0.02^{+0.09}_{-0.12}$	$0.07^{+0.09}_{-0.10}$	$-0.15^{+0.16}_{-0.18}$
[Fe/H]	$0.05^{+0.10}_{-0.17}$	$-0.06^{+0.17}_{-0.16}$	$-0.53^{+0.16}_{-0.30}$	$-0.25^{+0.14}_{-0.12}$	$-0.33^{+0.21}_{-0.13}$	$-0.25^{+0.15}_{-0.13}$	$-0.18^{+0.15}_{-0.30}$
[Mg/Fe]	$0.18^{+0.17}_{-0.09}$	$0.59^{+0.26}_{-0.31}$	$0.48^{+0.29}_{-0.20}$	$0.49^{+0.12}_{-0.11}$	$0.59^{+0.16}_{-0.15}$	$0.33^{+0.15}_{-0.10}$	$0.43^{+0.24}_{-0.17}$
[Na/Fe]	$-0.16^{+0.25}_{-0.27}$	$-0.07^{+0.17}_{-0.24}$	$-0.11^{+0.74}_{-0.27}$	$0.87^{+0.19}_{-0.16}$	$0.92^{+0.18}_{-0.21}$	$0.31^{+0.22}_{-0.20}$	$0.03^{+0.59}_{-0.40}$
[Ca/Fe]	$-0.12^{+0.17}_{-0.10}$	$0.08^{+0.20}_{-0.15}$	$0.18^{+0.28}_{-0.17}$	$0.35^{+0.09}_{-0.15}$	$0.36^{+0.13}_{-0.18}$	$0.07^{+0.11}_{-0.15}$	$0.17^{+0.20}_{-0.27}$
[O, Ne, S/Fe]	$-0.24^{+0.32}_{-0.28}$	$0.61^{+0.25}_{-0.47}$	$0.25^{+0.47}_{-0.34}$	$0.56^{+0.28}_{-0.52}$	$0.29^{+0.33}_{-0.26}$	$0.81^{+0.15}_{-0.18}$	$0.15^{+0.51}_{-0.43}$
[Ti/Fe]	$-0.09^{+0.36}_{-0.24}$	$0.67^{+0.18}_{-0.39}$	$0.51^{+0.37}_{-0.32}$	$0.23^{+0.33}_{-0.26}$	$0.64^{+0.22}_{-0.33}$	$0.02^{+0.31}_{-0.16}$	$0.22^{+0.46}_{-0.37}$
[C/Fe]	$-0.16^{+0.24}_{-0.18}$	$0.17^{+0.20}_{-0.19}$	$0.14^{+0.28}_{-0.31}$	$0.26^{+0.18}_{-0.15}$	$0.24^{+0.16}_{-0.19}$	$0.22^{+0.16}_{-0.16}$	$0.03^{+0.33}_{-0.22}$
[K/Fe]	$-0.35^{+0.32}_{-0.10}$	$0.15^{+0.31}_{-0.21}$	$0.05^{+0.31}_{-0.26}$	$0.24^{+0.25}_{-0.21}$	$0.16^{+0.26}_{-0.20}$	$0.19^{+0.28}_{-0.17}$	$0.21^{+0.21}_{-0.31}$
f_{dwarf} (per cent)	$7.00^{+5.31}_{-2.63}$	$4.47^{+3.52}_{-1.43}$	$3.96^{+4.84}_{-1.04}$	$7.18^{+3.10}_{-2.86}$	$8.56^{+4.43}_{-3.00}$	$4.53^{+3.75}_{-1.29}$	$8.59^{+5.40}_{-4.16}$
M/L	$1.27^{+0.84}_{-0.33}$	$0.93^{+0.49}_{-0.15}$	$0.89^{+0.65}_{-0.12}$	$1.35^{+0.47}_{-0.40}$	$1.34^{+0.77}_{-0.31}$	$0.99^{+0.53}_{-0.17}$	$0.97^{+1.03}_{-0.17}$

These results are presented in graphical form for key parameters in Fig. 8.

5.3 Analysis of results

5.3.1 [O, Ne, S/Fe]

In the full fit, we marginalize over the nuisance parameter [O, Ne, S/Z] which captures the (small) model variations due to variations in poorly constrained α -elements. As with other abundance parameters, we convert this to the more informative form [O, Ne, S/Fe]. As is clear from Fig. 5, the inferred values of

[O, Ne, S/Fe] are extremely high, albeit poorly constrained. Whilst the expected enhancement should be similar to that of [Mg/Fe], the most probable values appear to be systematically offset by approximately 1σ . This appears to be driven by the Na I 0.82 μm feature, which can be weakened somewhat by large values of this parameter, reducing the tension with the redder Na I feature strengths. In Table 11, we present the results of fitting the stacks without this parameter (assuming [O, Ne, S/Fe] = 0 instead). This allows us to show that the principal knock-on effect of including the [O, Ne, S/Fe] parameter is to increase the inferred [Na/Fe] value, since larger values can be reconciled with the Na I 0.82 μm feature's strength. The effect on the IMF is negligible.

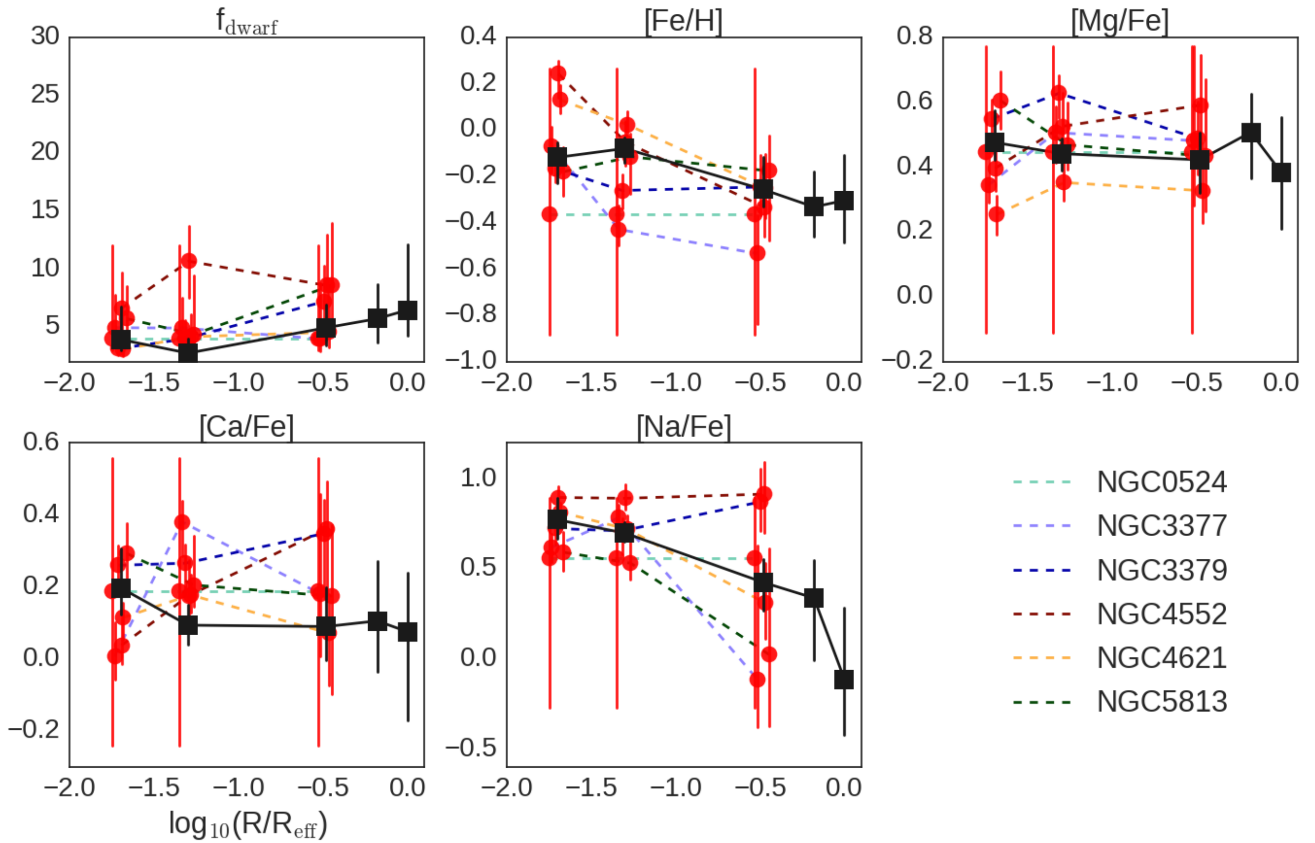


Figure 8. Stellar population fitting results for individual galaxies (red circles) as well as the stack (black squares). The fit incorporates the K -band data were available and shows the behaviour of key (well-constrained) parameters. We exclude NGC 1407 and NGC 4486, as without good-quality optical data the fits are not well-constrained.

Table 11. Estimated parameter values for the stacked spectra, acquired using the updated models and the full set of index measurements. In this table, the nuisance parameter [O, Ne, S/Fe] has been excluded from the fit. R1 and R2 correspond to the two extraction regions in the central IFU (<0.7 arcsec, >0.7 arcsec), whilst R3, R4, and R5 correspond to the rings of IFUs arranged at $\sim 1/3 R_{\text{eff}}$, $\sim 2/3 R_{\text{eff}}$, and $\sim R_{\text{eff}}$.

	R1	R2	R3	R4	R5	Gradient
Age /Gyr	$8.73^{+1.01}_{-0.88}$	$7.34^{+0.89}_{-0.23}$	$7.17^{+1.32}_{-0.12}$	$7.38^{+2.33}_{-0.25}$	$7.88^{+2.35}_{-0.59}$	-0.71 ± 0.55
X1	$1.79^{+0.70}_{-0.51}$	$1.81^{+0.49}_{-0.56}$	$1.60^{+0.70}_{-0.38}$	$1.13^{+1.14}_{-0.09}$	$1.32^{+1.40}_{-0.22}$	-0.32 ± 0.23
X2	$1.19^{+0.87}_{-0.13}$	$1.08^{+0.51}_{-0.05}$	$1.16^{+0.61}_{-0.11}$	$1.17^{+0.98}_{-0.11}$	$1.58^{+1.07}_{-0.37}$	0.14 ± 0.14
[Z/H]	$0.17^{+0.03}_{-0.03}$	$0.24^{+0.02}_{-0.03}$	$0.15^{+0.03}_{-0.04}$	$0.03^{+0.06}_{-0.09}$	$-0.14^{+0.11}_{-0.10}$	-0.09 ± 0.03
[Fe/H]	$-0.04^{+0.05}_{-0.07}$	$-0.07^{+0.04}_{-0.06}$	$-0.26^{+0.11}_{-0.08}$	$-0.3^{+0.15}_{-0.11}$	$-0.19^{+0.17}_{-0.21}$	-0.16 ± 0.05
[Mg/Fe]	$0.49^{+0.08}_{-0.04}$	$0.48^{+0.05}_{-0.04}$	$0.48^{+0.08}_{-0.08}$	$0.50^{+0.11}_{-0.13}$	$0.30^{+0.21}_{-0.16}$	-0.02 ± 0.04
[Na/Fe]	$0.63^{+0.09}_{-0.11}$	$0.64^{+0.05}_{-0.05}$	$0.32^{+0.13}_{-0.15}$	$0.06^{+0.26}_{-0.23}$	$-0.24^{+0.40}_{-0.27}$	-0.37 ± 0.09
[Ca/Fe]	$0.13^{+0.08}_{-0.06}$	$0.06^{+0.06}_{-0.05}$	$0.10^{+0.08}_{-0.10}$	$0.10^{+0.11}_{-0.17}$	$-0.12^{+0.20}_{-0.18}$	-0.05 ± 0.05
[C/Fe]	$0.06^{+0.09}_{-0.09}$	$0.11^{+0.06}_{-0.06}$	$0.21^{+0.08}_{-0.12}$	$0.17^{+0.14}_{-0.15}$	$-0.01^{+0.21}_{-0.24}$	0.06 ± 0.05
[Ti/Fe]	$0.52^{+0.13}_{-0.13}$	$0.36^{+0.09}_{-0.1}$	$0.37^{+0.17}_{-0.21}$	$0.62^{+0.19}_{-0.34}$	$0.48^{+0.30}_{-0.55}$	-0.02 ± 0.11
[K/Fe]	$0.06^{+0.21}_{-0.10}$	$0.06^{+0.10}_{-0.05}$	$0.2^{+0.21}_{-0.14}$	$0.20^{+0.26}_{-0.20}$	$0.13^{+0.27}_{-0.26}$	0.09 ± 0.07
f_{dwarf} (per cent)	$4.2^{+2.7}_{-1.1}$	$3.0^{+1.7}_{-0.6}$	$4.0^{+1.8}_{-1.1}$	$4.3^{+3.1}_{-1.3}$	$6.3^{+4.7}_{-2.5}$	0.7 ± 1.3
M/L	$0.89^{+0.39}_{-0.11}$	$0.79^{+0.23}_{-0.07}$	$0.83^{+0.28}_{-0.08}$	$0.91^{+0.45}_{-0.14}$	$0.96^{+0.84}_{-0.17}$	0.04 ± 0.08

5.3.2. $\text{Mg I } 0.88 \mu\text{m}$

As mentioned above, in the updated model framework it is challenging to fit our measurements of the $\text{Mg I } 0.88 \mu\text{m}$ feature, and so we did not include this feature in the fits so as to avoid biasing them. In Fig. 9, we show an index–index plot for the stack measure-

ments; we also show the model grids under variation of metallicity and [Mg/Fe] for a bottom-light and a bottom-heavy IMF. The data appear offset from the model grid.

An examination of the $\text{Mg I } 0.88 \mu\text{m}$ line in Fig. 7 suggests that the issue could be related to the pseudo-continuum definition

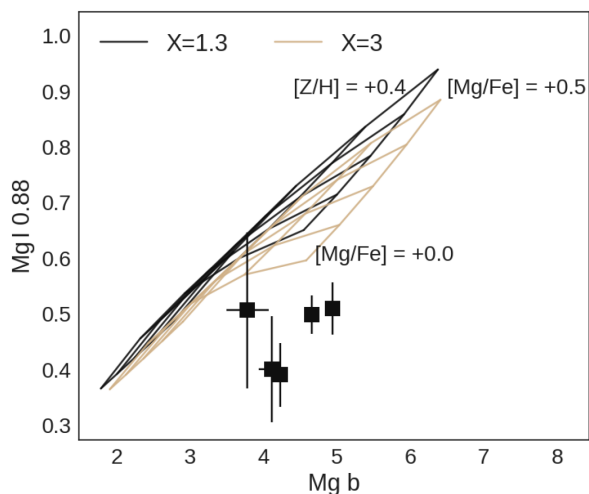


Figure 9. Equivalent widths (Å) of the Mg features, measured on the stacked spectra, along with model grids where the vertices indicate variation of metallicity and [Mg/Fe]. IMF variation makes relatively little difference to these features. The data and grids appear to be offset from each other.

in conjunction with differences between the model and the data in terms of long range spectral variations. On the red side of the feature, the pseudo-continuum band could be affected by the Ti I 0.89 μ m break.

5.3.3 [Na/Fe]

As in Paper I, the recovered sodium abundance is often very high. Once again, there is tension in the best-fitting model between the various Na I features. Examination of Fig. 6 suggests that the model tends to overestimate the strength of Na I 0.82 μ m and underestimate the strength of Na I 2.21 μ m.

As was discussed in Smith et al. (2015b), the Na I 1.14 μ m line has been found to be unusually strong in massive ETGs, which is difficult to reconcile with the SSP models without violating other constraints. Our finding of a discrepancy between the Na I 0.82 μ m and Na I 2.21 μ m lines indicates that the Na I 2.21 μ m line is similarly (or perhaps even *more*) discrepant. This contrasts with the findings of La Barbera et al. (2017), in which two massive ETGs were studied. The authors found that a different set of stellar population models that include *coupled* spectral responses to changes in the IMF and Na abundance are able to simultaneously match the strength of the Na I lines.

The discrepancy is shown particularly clearly in Fig. 10, which shows three index–index plots for the stacked spectra. Na I 0.82 μ m is comparatively insensitive to [Z/H] and is best fit with a fairly low [Na/Fe] in all cases. By contrast, the other two lines require *either* extremely high [Z/H] or [Na/Fe] (in the case of Na I 1.14 μ m, the required [Z/H] would be prohibitively high). We may also examine the relevant panels in Fig. 7, which shows the features from the centrally extracted stacked spectrum alongside the models. Na I 0.82 μ m can be reproduced by the more complex model, but as just discussed is weaker than can be accounted for with the simpler model. Na I 1.14 μ m is reproduced by both models, but Na 2.21 μ m appears discrepant in shape on the blue side of the feature.

5.3.4 The IMF: bottom heavy or Milky Way like?

The CvD16 models allow the IMF additional flexibility, with the functional form modelled as a two-part broken power law with slope X1 below $0.5 M_{\odot}$ and X2 between 0.5 and $1.0 M_{\odot}$. In practice, this means that the relative contributions of the least massive stars and the $\sim 0.5 M_{\odot}$ stars can be varied separately – in reality, of course, varying the upper slope X2 will increase/decrease the contribution of both, so the two parameters have some degeneracy.

For the stacked spectra, the IMF we recover is consistent with the Milky Way IMF in all cases (in contrast to Paper I, where a modestly bottom heavy IMF was preferred). The individual galaxies show scatter of ~ 2 per cent in f_{dwarf} around a mean of 5.6 per cent (where a Kroupa IMF corresponds to $f_{\text{dwarf}} = 5$ per cent) and in almost all cases are consistent with this mean value within the estimated statistical uncertainties. The individual galaxies appear offset from the stack in one case: this may be indicative of unaccounted-for systematics (the [Ca/Fe] abundance shows an offset at a similar level in the same bin).

Compared to the results presented in Paper I, however, the distribution of IMFs is considerably tighter than before and with the addition of new data and updated models we infer lower contributions to the light from dwarf stars (e.g. for the centrally extracted stack, 90 per cent of draws from the posterior probability distribution correspond to $f_{\text{dwarf}} < 8.4$ per cent, corresponding to the Salpeter IMF, whereas in Paper I we found $f_{\text{dwarf}} = 9.4 \pm 2.1$ per cent).

The relationship between the IMF slope/slopes and the index strengths is highly non-linear. We now discuss the consequences of this for the inferred parameters. In Fig. 11, we give as an example the joint and marginal posterior probability distributions over X1 and X2 inferred for the innermost spectrum of NGC 5813. The marginalized distributions of these two parameters are broad and somewhat skewed. Whilst some covariance between the two parameters remains, this is mitigated by the use of multiband data. To aid comparison, we plot three lines of constant f_{dwarf} . Whilst the form of the IMF varies between points on one of these lines, the chosen values of f_{dwarf} correspond to Milky Way-like, Salpeter, and $X = 3$ power-law IMFs respectively: most of the joint probability is enclosed between the first two of these.

In Fig. 12, we transform this distribution into the posterior probability for f_{dwarf} and relative M/L. These parameters are quite strongly correlated, as is clear from the figure. Note that the posterior probability distributions are less skewed than for X1, X2 (as might be anticipated from the roughly linear dependence of f_{dwarf} on the index strengths, which have symmetric statistical uncertainties). Crucially, these distributions are more strongly peaked because of the non-linear response of the index strengths to the IMF slope. Expressed another way, the plateau in the X1 posterior distribution is due to the fact that the indices change little for variations in that range (and neither does f_{dwarf}). It is therefore not immediately clear from the individual most probable values of X1 and X2 whether or not we find a bottom-heavy IMF, whereas examination of the joint distribution, or the f_{dwarf} distribution does indicate a modestly bottom-heavy IMF (though nevertheless consistent with Milky Way like within the uncertainties). For this reason, we ensure that all results presented in this work include f_{dwarf} and relative M/L values as well as the constraints on the power-law slopes (whilst cautioning the reader that the most probable values quoted may not appear to agree in an intuitive way).

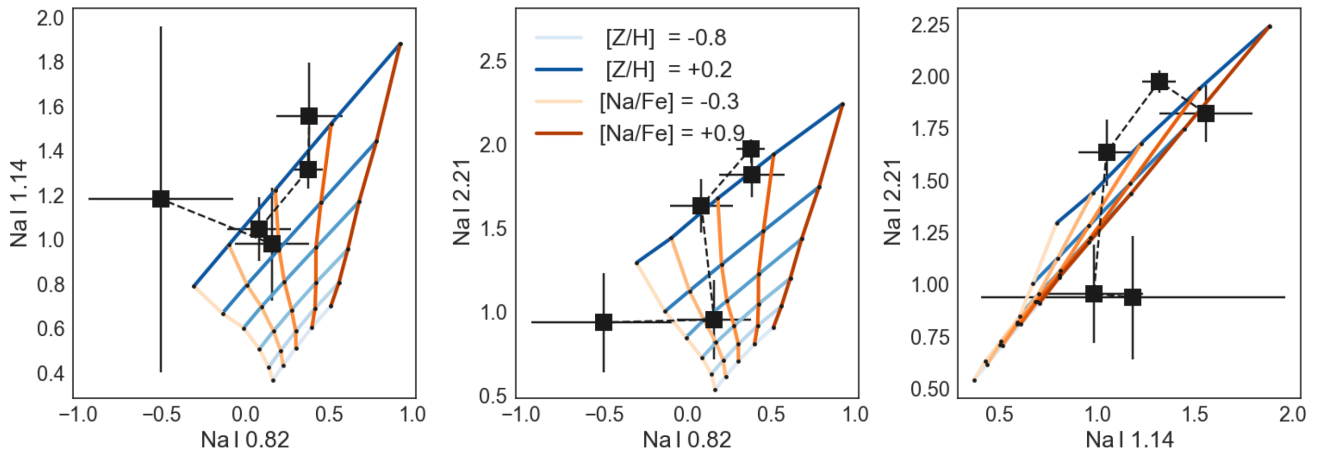


Figure 10. Equivalent widths of the Na features, measured on the stacked spectra, along with model grids where the vertices indicate variation of metallicity and [Na/Fe], assuming a Milky Way-like IMF. Blue lines are lines of constant [Z/H], orange lines are lines of constant [Na/Fe]. Darker colours indicate higher values. Finally, dashed lines link data points from adjacent radial extraction zones.

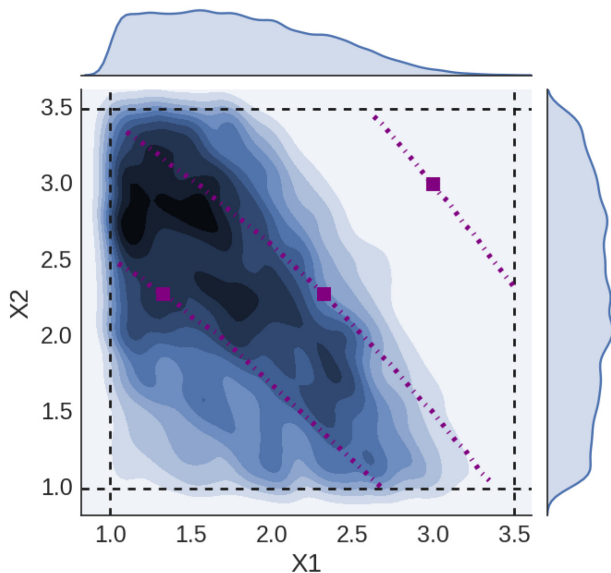


Figure 11. The results of fitting feature strengths from the centrally extracted spectrum from NGC 5813 with X_1 and X_2 varying freely. The joint and marginal distributions are shown via kernel-density estimation. Prior boundaries are indicated by the thick dashed lines, whilst dot-dashed contours indicate three lines of constant $f_{\text{dwarf}} = 5.0, 8.4,$ and 19.0 percent (bottom left to top right). These values are equal to f_{dwarf} in the case of Kroupa, Salpeter, and $X = 3$ IMFs, respectively. Square markers show the location of these particular IMFs on each line.

5.3.5 Shape of the IMF

Spectroscopic techniques for constraining the IMF are fairly insensitive to the functional form of the IMF, principally measuring the fractional contribution to the total light from dwarf stars. None the less, given measurements of a wide set of absorption indices with sensitivities to different stellar mass ranges (as in this work), some information about the IMF shape can, in principle, be recovered. In practice, some covariance between the IMF broken power-law slopes X_1 and X_2 remains, meaning the signal is weak. In Fig. 13, we show the posterior probability distribution of the quantity $X_2 - X_1$, a quantity which we use here as a proxy for IMF shape. The larger this quantity, the more sharply the IMF turns over at

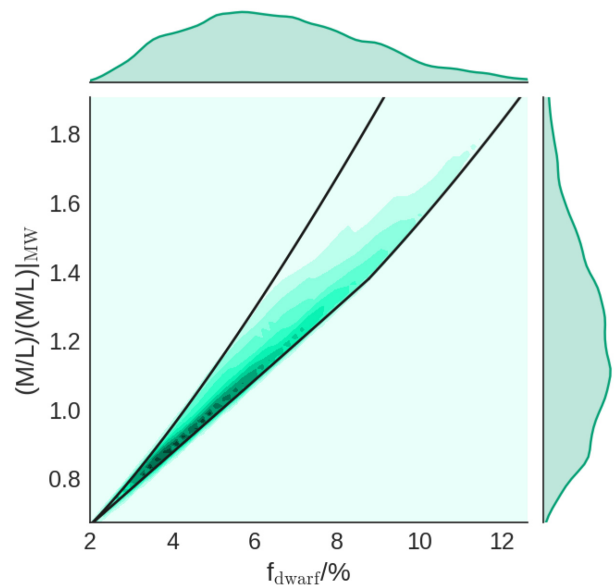


Figure 12. This plot corresponds to Fig. 11, with the inferred posterior distribution of X_1 and X_2 for NGC 5813 recast into values of f_{dwarf} and V-band M/L (normalized so that $M/L = 1$ for a Milky Way-like population). The thick black line corresponds to the region enclosed by the priors on X_1 and X_2 .

low stellar masses. Lines of constant $X_2 - X_1$ lie approximately orthogonal to lines of constant f_{dwarf} in the (X_1, X_2) plane (e.g. Fig. 11). For a Milky Way IMF $X_2 - X_1 = 1$, whilst for a single power law such as the Salpeter IMF it is zero. Whilst some studies have focused on single power laws, others, e.g. La Barbera et al. (2016), explore bottom-heavy IMFs with $X_1 = 1.3$ (as in the Milky Way) and $X_2 > 2.3$, i.e. $X_2 - X_1 > 1$. For the stacked spectra, this proxy for IMF shape is not well constrained, but appears to prefer (at a marginal level) IMFs that break less sharply at low mass. However, this is because with poor constraints on the IMF shape the marginalized distribution reflects the imposed prior. MCMC walkers exploring low f_{dwarf} regions are constrained more tightly in $X_2 - X_1$ around zero, so if f_{dwarf} is not well constrained in the middle of the prior box then when we f_{dwarf} marginalize over the full posterior distribution more walkers will be found in the vicinity of $X_2 -$

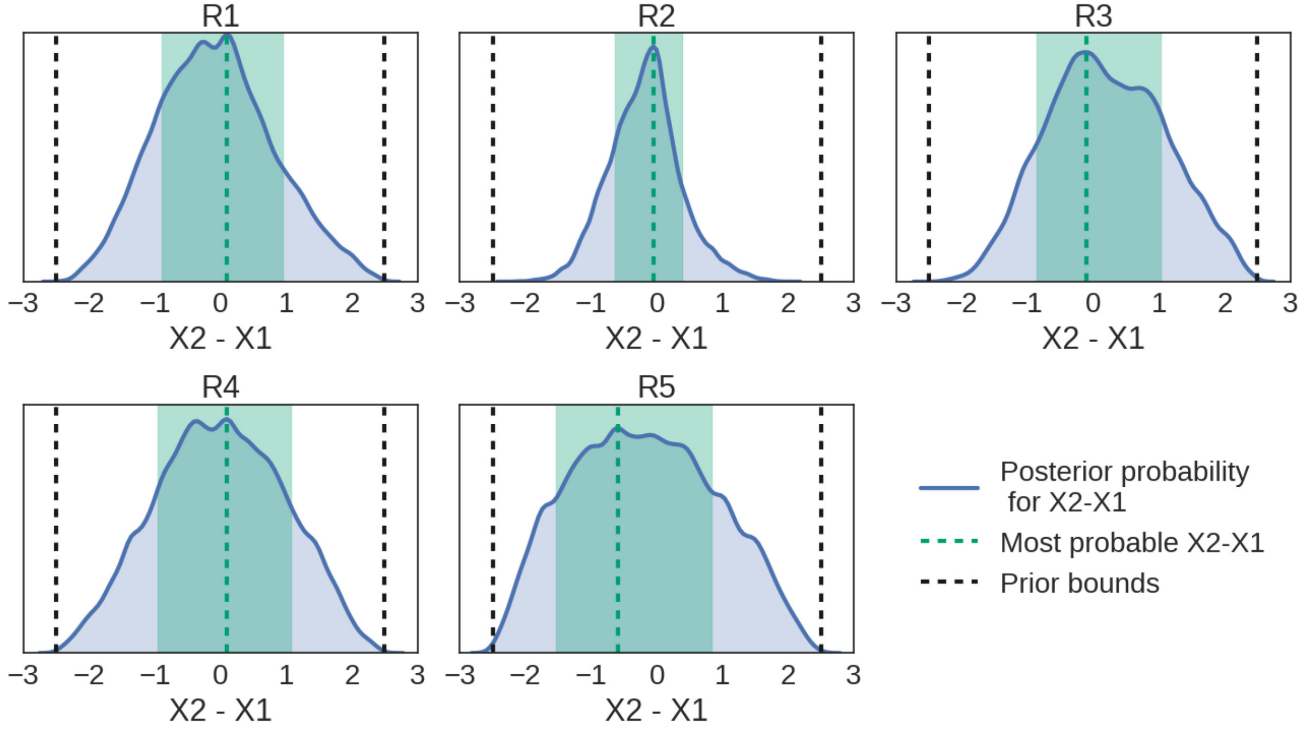


Figure 13. This plot indicates our constraints on the shape of the IMF via the difference in the power-law slopes $X1$ and $X2$. The kernel density estimates show the posterior probability distributions of this quantity for the five stacked spectra. For the Milky Way IMF, $X2 - X1 = 1$, whereas for a single power law (e.g. the Salpeter IMF) it is zero. The signal is weak since the IMF-dependent changes to spectral features principally track f_{dwarf} . Because of this, the posterior distributions reflect the imposed prior on $X1$ and $X2$, a point we explore in more detail in Appendix C.

$X1 = 0$ than if we had drawn uniformly from $[f, X2 - X1]$ instead. Note that in the work presented in [Paper I](#) we explicitly made use of a uniform prior in f_{dwarf} , whilst $X2 - X1$ was implicitly fixed to zero.

5.3.6 Effect of the prior on inference of the IMF

Evaluation of the posterior probability distribution for the IMF requires that a prior probability distribution be specified. In the work, we have presented so far, we have assumed an equal prior probability for any value of $X1$ and $X2$ within set limits. This is not the only possible choice; an alternative would be to assume equal prior probability for any value of f_{dwarf} within certain limits and likewise for our proxy for IMF shape, $X2 - X1$. Such a prior is very far from uniform in $X1, X2$.

In Fig. 14, we demonstrate the difference between these two scenarios. The plot shows the density of points randomly and uniformly drawn from $X1$ and $X2$ within the bounds of the prior in f_{dwarf} , $X2 - X1$ space as well as estimates of the marginalized distributions of these points, which we can identify with the corresponding prior on f_{dwarf} and $X2 - X1$. It is clear that this prior picks out preferred values for these quantities. Likewise, a uniform prior on these quantities would pick out preferred values of $X1, X2$. Note that in the work presented in [Paper I](#) we explicitly made use of a uniform prior in f_{dwarf} .

It is crucial to quantify the effect that our choice of prior may have on our results, so to this end we re-ran MCMC using a uniform prior on both f_{dwarf} and $X2 - X1$. It is important to note that this requires us to explore a more restricted parameter space (4 per cent $< f_{\text{dwarf}} < 15$ per cent, $-1.5 < X2 - X1 < 1.5$) in order to remain within the CvD16 model grids. The results for most param-

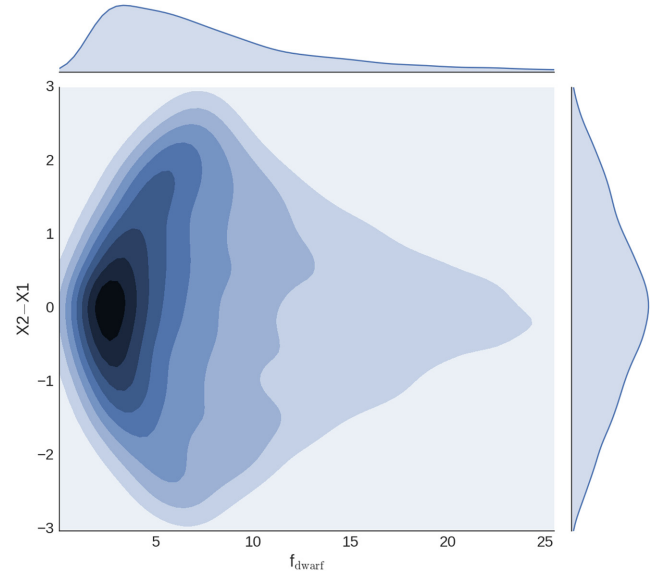


Figure 14. Density distribution in f_{dwarf} versus $X2 - X1$ space for points drawn uniformly from $0.5 < X1, X2 < 3.5$. This demonstrates that a prior probability distribution on $X1$ and $X2$ which is uniform between some limits (in this case, $0.5 < X1, X2 < 3.5$) corresponds to a peaked distribution in both f_{dwarf} and $X2 - X1$.

eters are unchanged, but the prior unsurprisingly has an effect on the most probable values of the IMF parameters. In Fig. 15, we show the marginalized posterior distributions for $X2 - X1$ computed for each of the stacked spectra.

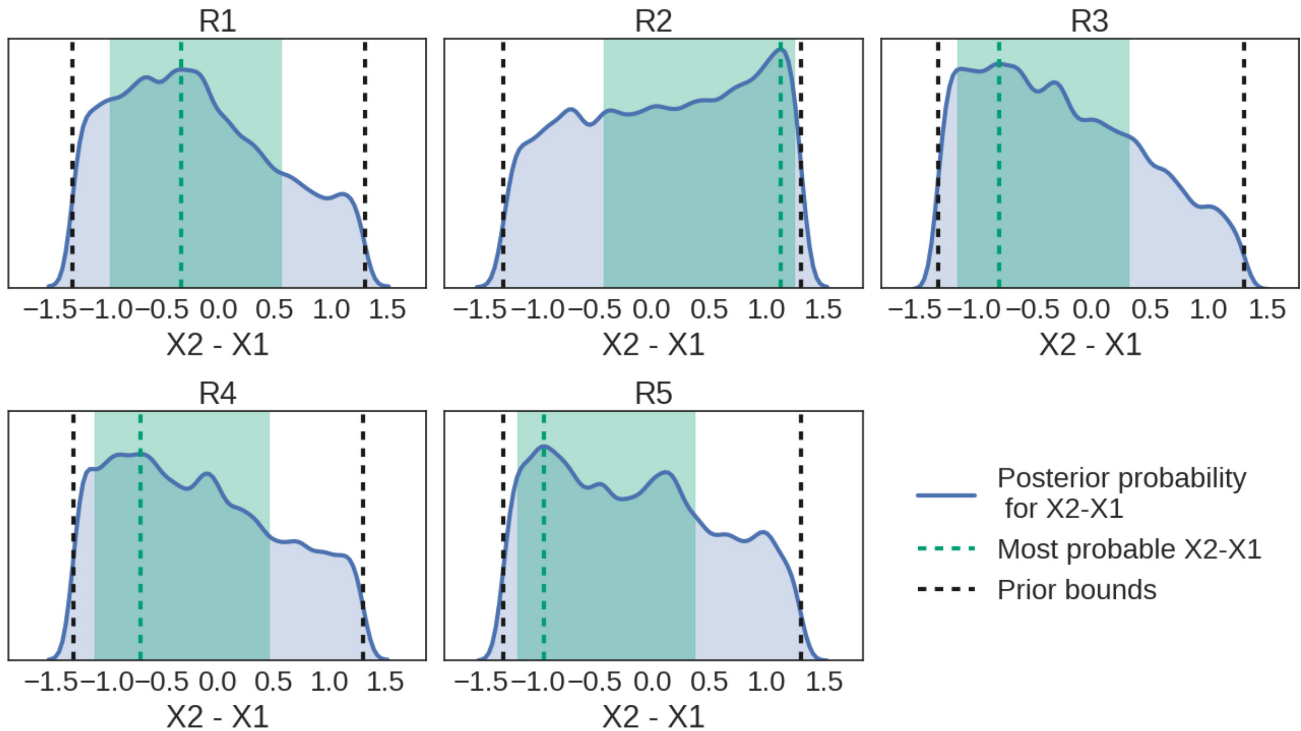


Figure 15. This plot indicates our constraints on the shape of the IMF via the difference in the power-law slopes $X1$ and $X2$. The kernel density estimates show the posterior probability distributions of this quantity for the five stacked spectra. For the Milky Way IMF, $X2 - X1 = 1$, whereas for a single power law (e.g. the Salpeter IMF) it is zero. The signal is weak, since the IMF-dependent changes to spectral features principally track f_{dwarf} . Because of this, the posterior distributions reflect the imposed prior on $X1$ and $X2$; in contrast to Fig. 13, a uniform prior on $X2 - X1$ has been used here.

This makes clear that in some cases the evidence provided by our data (as averaged in the stacked spectra) generally favours IMFs that steepen at low stellar masses, but not decisively so. For Kroupa, $X2 - X1 = 1$, which in the innermost stacked spectrum is somewhat in tension with the data (about 5 per cent of draws from the posterior distribution have $X2 - X1 > 1$). On the other hand, whereas in Fig. 13 the stack from the next extraction region out appeared to decisively exclude the Kroupa shape, Fig. 15 shows that the data are completely unable to constrain the shape under our alternative prior. It is clear that any attempt to extract information about the IMF shape from spectroscopic data must pay close attention to the chosen prior probability distribution.

In Table 12, we show how our results are modified using the alternative prior. This approach yields somewhat more bottom-heavy IMFs, which are none the less consistent with Kroupa (for which $f_{\text{dwarf}} \simeq 5$ per cent). In the central extraction region, the inferred f_{dwarf} and $X2 - X1$ would also be consistent with a Salpeter single power law, similar to the result obtained in Paper I (in which a prior that was uniform in f_{dwarf} was used).

Finally, in Fig. 16 we show an equivalent plot to Fig. 11 but with the inference carried out under a prior that is uniform in f_{dwarf} and $X2 - X1$. The results for this spectrum are comparable: a modestly bottom heavy IMF is preferred, albeit one that steepens rather than flattens at lower stellar mass (note that the shapes are none the less consistent, given the uncertainties).

6 DISCUSSION

We have measured the radially varying strengths of several K -band absorption lines for seven of the eight ETGs in the KINETyS sample, finding a significant gradient in the strength of the NaI 2.21 μm line

and rather flat radial profiles for the Ca I features at 1.98 and 2.26 μm and also the CO bandhead at 2.30 μm .

Using the CvD16 SSP models and our own code for stellar population parameter fitting, we extended the work presented in Paper I. Our results are broadly consistent with those previously presented, but the more extensive parameter coverage of the new models – combined with the additional data – allow us to place better constraints on the IMF and chemical abundance properties of our sample than was previously possible.

As in Paper I, we do not find strong evidence for IMF variations in our sample of galaxies, either on average (via the stacked data) or in individual galaxies. Indeed, the new parameter fits generally favour Milky Way-like IMFs and provide little evidence for an IMF gradient. Moreover, we now model the IMF as a two-part power law, mitigating any issues that might have arisen from our previous single parameter treatment, though at the expense of some additional ambiguity in the interpretation of the results. Our results contrast with e.g. van Dokkum et al. (2017), in which the IMF was found to be typically very bottom heavy ($f_{\text{dwarf}} > 20$ per cent) in the core regions of ETGs and consistent with Milky Way like at half the effective radius. On the other hand, they are not dissimilar from those in La Barbera et al. (2017), in which two ETGs are studied and found (using an IMF model assumed to flatten below $0.5M_{\odot}$) to have more modestly bottom-heavy IMFs in their core regions ($f_{\text{dwarf}} \gtrsim 8.4$ per cent). Given the sensitivity of our results to the prior on the IMF, this level of IMF variation is not necessarily inconsistent with our findings.

As stellar population synthesis models have become more sophisticated, especially with respect to their treatment of the IMF functional form, it has become apparent that IMF variations may be quite subtle in many cases. For example, Newman et al. (2017)

Table 12. Estimated parameter values for the stacked spectra, acquired using the updated models and the full set of index measurements. For the IMF, we fit a two-part power law with slopes X1 and X2, but used a prior distribution that was uniform in f_{dwarf} and $X2 - X1$ (instead of in X1 and X2). We also fit for stellar population age and total metallicity, as well as the abundances of various elements of interest (we note that the IMF prior has negligible impact on these).

	R1	R2	R3	R4	R5	Gradient
Age /Gyr	$10.75^{+1.39}_{-1.43}$	$8.82^{+0.92}_{-0.68}$	$8.47^{+1.70}_{-0.90}$	$7.50^{+3.33}_{-0.32}$	$8.86^{+2.25}_{-1.22}$	-1.09 ± 0.64
f_{dwarf} (per cent)	$6.8^{+3.4}_{-1.9}$	$4.2^{+0.9}_{-0.1}$	$4.9^{+2.9}_{-0.6}$	$6.8^{+4.0}_{-1.9}$	$10.0^{+3.1}_{-3.8}$	1.7 ± 1.9
X2-X1	$-0.33^{+0.89}_{-0.63}$	$1.13^{+0.12}_{-1.55}$	$-0.79^{+1.11}_{-0.35}$	$-0.70^{+1.16}_{-0.41}$	$-0.95^{+1.32}_{-0.23}$	-0.06 ± 0.50
[Z/H]	$0.15^{+0.04}_{-0.04}$	$0.23^{+0.02}_{-0.02}$	$0.13^{+0.04}_{-0.06}$	$0.05^{+0.06}_{-0.13}$	$-0.04^{+0.08}_{-0.16}$	-0.06 ± 0.04
[Fe/H]	$-0.18^{+0.08}_{-0.10}$	$-0.11^{+0.04}_{-0.06}$	$-0.19^{+0.09}_{-0.13}$	$-0.34^{+0.16}_{-0.11}$	$-0.21^{+0.16}_{-0.20}$	-0.08 ± 0.05
[Mg/Fe]	$0.57^{+0.07}_{-0.08}$	$0.45^{+0.05}_{-0.04}$	$0.46^{+0.07}_{-0.11}$	$0.50^{+0.09}_{-0.14}$	$0.35^{+0.18}_{-0.17}$	-0.05 ± 0.04
[Na/Fe]	$0.84^{+0.09}_{-0.13}$	$0.71^{+0.06}_{-0.05}$	$0.41^{+0.14}_{-0.14}$	$0.25^{+0.23}_{-0.31}$	$-0.17^{+0.42}_{-0.26}$	-0.41 ± 0.08
[Ca/Fe]	$0.24^{+0.11}_{-0.07}$	$0.11^{+0.06}_{-0.05}$	$0.15^{+0.09}_{-0.11}$	$0.15^{+0.11}_{-0.16}$	$-0.08^{+0.25}_{-0.17}$	-0.06 ± 0.04
	$0.83^{+0.12}_{-0.22}$	$0.67^{+0.08}_{-0.09}$	$0.80^{+0.12}_{-0.16}$	$0.76^{+0.23}_{-0.26}$	$0.65^{+0.23}_{-0.31}$	0.03 ± 0.06
[O, Ne, S/Fe]						
[C/Fe]	$0.22^{+0.15}_{-0.11}$	$0.13^{+0.08}_{-0.05}$	$0.20^{+0.13}_{-0.12}$	$0.27^{+0.14}_{-0.17}$	$0.10^{+0.19}_{-0.25}$	0.03 ± 0.04
[Ti/Fe]	$0.61^{+0.20}_{-0.15}$	$0.32^{+0.10}_{-0.11}$	$0.23^{+0.20}_{-0.23}$	$0.53^{+0.22}_{-0.27}$	$0.38^{+0.35}_{-0.45}$	-0.07 ± 0.09
[K/Fe]	$0.19^{+0.19}_{-0.11}$	$0.10^{+0.09}_{-0.06}$	$0.20^{+0.17}_{-0.15}$	$0.14^{+0.25}_{-0.17}$	$0.28^{+0.23}_{-0.38}$	0.05 ± 0.08

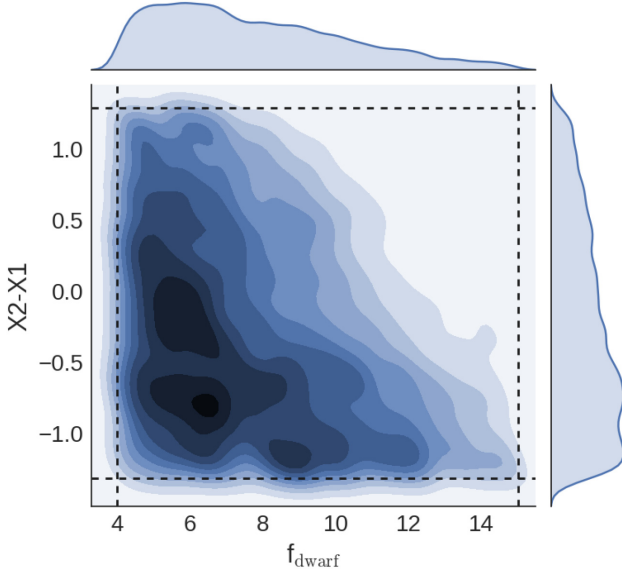


Figure 16. The results of fitting feature strengths from the centrally extracted spectrum from NGC 5813 with a uniform prior on f_{dwarf} and $X2 - X1$ (corresponds to Fig. 11, other than the change to the prior). The joint and marginal distributions are shown via kernel-density estimation. Prior boundaries are indicated by the thick dashed lines. The results are consistent; a somewhat bottom-heavy IMF is recovered.

showed that a stacked spectrum derived from observations of high-mass ETGs ($\sigma \simeq 280 \text{ km s}^{-1}$) can, when modelled with a flexible IMF model consisting of a two-part power law and a variable low-mass cut-off, be reproduced with only a modest enhancement in stellar M/L (or f_{dwarf}). The same observations require a power law with a steeper-than-Salpeter slope if a single-slope IMF with fixed low-mass cut-off is assumed. Moreover, Newman et al. show that a model with such a flexible IMF can significantly reduce the tension between results from spectroscopy and from lensing measurements for the three lensed ETGs with Milky Way-like M/L presented in Smith, Lucey & Conroy (2015a). If these fairly modest enhancements to the dwarf star content of ETGs are typical, the contribution of dwarf stars to the integrated light may be increased by only 1 or

2 per cent in the majority of galaxies, which would be consistent with our findings here.

Concerning the recovered abundance gradients, in our new formalism we fit explicitly for total metallicity and then consider the variations of particular elements on top of this trend. On average, we find strong [Na/Fe] radial gradients in our sample, i.e. [Na/H] ramps up in the core faster than the overall metallicity trend would predict (by contrast, whilst Mg and perhaps Ca are enhanced, they are superabundant by a constant factor with respect to Fe throughout). This lends credence to our suggestion, first made in Paper I, that the metallicity-dependent yield of Na is playing a role in these galaxies. The extreme [Na/H] values we infer (typically 0.5–0.6 in the central extraction regions of the KINeTyS sample, consistent with the result from the stacked spectrum for this region) potentially pose a challenge; SSP models must rely on theoretical predictions rather than empirical spectra since metal-rich stars so superabundant in Na are not observed in the Milky Way.

Our results indicate some tension between the measurements of different Na lines, which might be accounted for by a modelling issue of this kind. In Fig. 10, we showed how for the stacked spectra the Na I 0.82 μm line strength at face value appears to prefer lower values of [Na/Fe]. Index versus index grids should be treated with caution due to the cumulative minor effects of various unaccounted-for parameters. For example, in this case the inclusion of a [Ti/Fe] parameter (as in the more complex model presented above) can reduce the tension significantly, though not entirely. This is because Na I 0.82 μm lies within a broad Ti absorption band. The effect of this enhanced Ti is to weaken the measured equivalent width somewhat. This and other parameters can therefore help to reconcile the measurements by allowing weaker Na I 0.82 μm at higher [Na/Fe]. Nevertheless, some systematic tension remains between the three infrared Na I features, which may be partially due to the modelling of these features in highly Na-enhanced populations (but see La Barbera et al. 2017).

Proper constraints on [Na/Fe] are crucial, as Na abundance has important effects on the strength of other indices, in particular the Wing-Ford band. In Fig. 17, we show how this effect can explain the radial behaviour of the Wing-Ford band in the stacked KMOS spectra. The same figure also shows that it would be challenging to reconcile this measurement with a systematically bottom-heavy

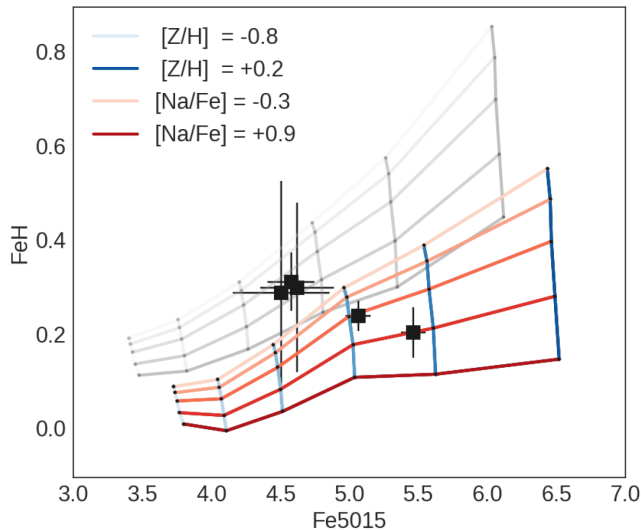


Figure 17. Index–index grid for the optical Fe 5015 index and the Wing-Ford (FeH) band, computed at $[\alpha/\text{Fe}] = +0.5$ for a Kroupa IMF. The KMOS data are superimposed in black. The stacked measurements of the Wing-Ford band are weakest for the innermost extraction region (e.g. see Fig. 6), consistent with the strongly increasing Na abundance, which barely affects Fe 5015 but has a significant effect on the Wing-Ford band. Note that a more bottom-heavy IMF would tend to make FeH stronger whilst leaving Fe 5015 largely unchanged – the shift for a Salpeter single power law is indicated by the offset light grey grid – so would require e.g. even more extreme Na abundance to match the KMOS measurements.

IMF in the cores of our sample galaxies, in contrast to the results of e.g. Martín-Navarro et al. (2015) and van Dokkum et al. (2017). Note, however, that an even more flexible IMF prescription that included a flexible low-mass cut-off in the IMF could help mitigate this tension, since the Wing-Ford band is principally sensitive to the lowest mass dwarf stars.

The Wing-Ford band in massive ETGs has undergone extensive study in recent years, e.g. by McConnell et al. (2016), Vaughan et al. (2018), Zieleniewski et al. (2017), and La Barbera et al. (2016). These studies find a range of values for the Wing-Ford (FeH) band, from 0.4 to 0.6 Å, whereas our measurements from KMOS data lie primarily between 0.2 and 0.3 Å. However, it is notable that e.g. Zieleniewski quantifies possible systematics affecting FeH and concludes that true values of the strength as low as 0.2–0.3 Å (at 200 km s^{−1} velocity dispersion) are not implausible; FeH is a weak feature and so is hard to measure accurately. Therefore, this tension may simply reflect the varying systematics, affecting different studies. In the case of our results, we do not find that removing FeH from consideration leads to more bottom-heavy IMFs being recovered (although of course the statistical uncertainty is on the value of f_{dwarf} is somewhat increased – by 6 per cent on average in the stacked spectra – without it).

7 CONCLUSIONS

We have built upon the work presented in Paper I in several important ways. First, we have deployed a significantly more advanced implementation of our stellar population parameter inference code. The updated code capitalizes on recent advances by using the state-of-the-art CvD16 stellar population models. These are based on a much-improved stellar spectral library and feature a more compre-

hensive set of stellar population parameters than the CvD12 models that we used previously, including the ability to model IMFs with different shapes and to vary the overall metallicity. Secondly, we have obtained K-band spectroscopy of almost all of the KINeTyS sample, allowing us to make measurements of previously underutilized spectral features as stellar population diagnostics. This adds significant discriminatory power to our method, allowing us to further break degeneracies between model parameters. Our conclusions are as follows:

(i) We used stacked spectra extracted from different radii within the KINeTyS sample to investigate the radial behaviour of four K-band spectral features. We found a strong decline in the strength of the Na I 2.21 μm line with radius (-0.53 ± 0.08 per decade in R/R_{eff}), and fairly constant strength for two Ca I features. The CO 2.30 μm a line likewise appears roughly constant in strength (-0.11 ± 0.13).

(ii) We use our updated stellar population spectral index fitting code in conjunction with these measurements to place additional constraints on the stellar populations of our sample. From the stacked spectra, we recover an average metallicity gradient $\Delta[Z/H]$ of -0.11 ± 0.03 per decade in R/R_{eff} and measure the abundances of several α -capture elements, finding flat trends in the relative abundances $[\text{Mg}/\text{Fe}]$, $[\text{Ca}/\text{Fe}]$, $[\text{Ti}/\text{Fe}]$, and $[\text{O}, \text{Ne}, \text{S}/\text{Fe}]$. The latter two parameters are not well constrained, but we find $[\text{Ca}/\text{Fe}]$ much less enhanced than $[\text{Mg}/\text{Fe}]$, consistent with our previous findings.

(iii) We find a very strong radial gradient in $[\text{Na}/\text{Fe}]$ of -0.35 ± 0.09 , a tighter constraint than that presented in Paper I, aided by our measurements of the Na I 2.21 μm line. However, there is mild tension between the absolute strengths of the three Na I features we measure, which may be a consequence of the theoretical modelling of Na line strengths in stellar populations where Na is superabundant. The extreme abundance of Na implied by our measurements in the cores of massive ETGs may be explained by the metallicity-dependent nucleosynthetic yield of Na.

(iv) For the IMF, we infer a Milky Way-like, non-radially varying IMF both for the stacked spectra and most of the individual galaxies in the sample.

Our results appear to indicate that the principal driver of radial spectroscopic variations is the abundance gradients created by the ETG formation process. On average, we infer that IMF variations in massive ETGs are subtle in most cases and we do not find compelling evidence for strong radial variations in the IMF in the inner regions. This stands in contrast to some recent results. In future, it will be important to compare constraints from different methods (e.g. spectroscopy and dynamics) in individual galaxies in order to address this tension.

ACKNOWLEDGEMENTS

This study is based on observations obtained at the Very Large Telescope of the European Southern Observatory, programme ID: 097.B-0882(A). PA was supported by an STFC studentship (ST/K501979/1) and RJS by the STFC Durham Astronomy Consolidated Grants 2014–2017 (ST/L00075X/1) and 2017–2020 (ST/P000541/1). The KMOS data used here are available through the ESO science archive.

The authors thank Charlie Conroy for providing the latest version of the CvD models.

REFERENCES

- Alton P. D., Smith R. J., Lucey J. R., 2017, *MNRAS*, 468, 1594 (Paper I)
- Auger M. W., Treu T., Gavazzi R., Bolton A. S., Koopmans L. V. E., Marshall P. J., 2010, *ApJ*, 721, L163
- Bastian N., Covey K. R., Meyer M. R., 2010, *ARA&A*, 48, 339
- Bezanson R., van Dokkum P. G., Tal T., Marchesini D., Kriek M., Franx M., Coppi P., 2009, *ApJ*, 697, 1290
- Cappellari M. et al., 2012, *Nature*, 484, 485
- Cappellari M., Emsellem E., 2004, *PASP*, 116, 138
- Cesetti M. et al., 2009, *A&A*, 497, 41
- Chabrier G., 2003, *PASP*, 115, 763
- Conroy C., van Dokkum P., 2012a, *ApJ*, 747, 69 (CvD12a)
- Conroy C., van Dokkum P. G., 2012b, *ApJ*, 760, 71 (CvD12b)
- Conroy C., Villaume A., van Dokkum P. G., Lind K., 2018, *ApJ*, 854, 139
- Davidge T. J., Beck T. L., McGregor P. J., 2008, *ApJ*, 677, 238
- Foreman-Mackey D., Hogg D. W., Lang D., Goodman J., 2013, *PASP*, 125, 306
- Goodman J., Weare J., 2010, *CAMCoS*, 5, 65
- Hilz M., Naab T., Ostriker J. P., 2013, *MNRAS*, 429, 2924
- Hopkins P. F., Bundy K., Murray N., Quataert E., Lauer T. R., Ma C.-P., 2009, *MNRAS*, 398, 898
- Hopkins P. F., Bundy K., Hernquist L., Wuyts S., Cox T. J., 2010, *MNRAS*, 401, 1099
- Kroupa P., 2001, *MNRAS*, 322, 231
- La Barbera F., Ferreras I., Vazdekis A., de la Rosa I. G., de Carvalho R. R., Trevisan M., Falcón-Barroso J., Ricciardelli E., 2013, *MNRAS*, 433, 3017
- La Barbera F., Vazdekis A., Ferreras I., Pasquali A., Cappellari M., Martín-Navarro I., Schönebeck F., Falcón-Barroso J., 2016, *MNRAS*, 457, 1468
- La Barbera F., Vazdekis A., Ferreras I., Pasquali A., Allende Prieto C., Röck B., Aguado D. S., Peletier R. F., 2017, *MNRAS*, 464, 3597
- Luhman K. L., Briceño C., Stauffer J. R., Hartmann L., Barrado y Navascués D., Caldwell N., 2003, *ApJ*, 590, 348
- Lyubenova M., Kuntschner H., Silva D. R., 2008, *A&A*, 485, 425
- Marks M., Kroupa P., Dabringhausen J., Pawłowski M. S., 2012, *MNRAS*, 422, 2246
- Mármol-Queraltó E. et al., 2009, *ApJ*, 705, L199
- Martín-Navarro I., Barbera F. L., Vazdekis A., Falcón-Barroso J., Ferreras I., 2015, *MNRAS*, 447, 1033
- McConnell N. J., Lu J. R., Mann A. W., 2016, *ApJ*, 821, 39
- McDermid R. M. et al., 2015, *MNRAS*, 448, 3484
- Meneses-Goytia S., Peletier R. F., Trager S. C., Vazdekis A., 2015, *A&A*, 582, A97
- Newman A. B., Smith R. J., Conroy C., Villaume A., van Dokkum P., 2017, *ApJ*, 845, 157
- Oser L., Ostriker J. P., Naab T., Johansson P. H., Burkert A., 2010, *ApJ*, 725, 2312
- Oser L., Naab T., Ostriker J. P., Johansson P. H., 2012, *ApJ*, 744, 63
- Rayner J. T., Cushing M. C., Vacca W. D., 2009, *ApJS*, 185, 289
- Salpeter E. E., 1955, *ApJ*, 121, 161
- Schiavon R. P., 2007, *ApJS*, 171, 146
- Sharples R. et al., 2013, *Messenger*, 151, 21
- Silva D. R., Kuntschner H., Lyubenova M., 2008, *ApJ*, 674, 194
- Smith R. J., Lucey J. R., 2013, *MNRAS*, 434, 1964
- Smith R. J., Lucey J. R., Carter D., 2012, *MNRAS*, 426, 2994
- Smith R. J., Lucey J. R., Conroy C., 2015a, *MNRAS*, 449, 3441
- Smith R. J., Alton P., Lucey J. R., Conroy C., Carter D., 2015b, *MNRAS*, 454, L71
- Spiniello C., Trager S. C., Koopmans L. V. E., Chen Y. P., 2012, *ApJ*, 753, L32
- Thomas D., Maraston C., Bender R., 2003, *MNRAS*, 339, 897
- Thomas J. et al., 2011, *MNRAS*, 415, 545
- van Dokkum P., Conroy C., Villaume A., Brodie J., Romanowsky A. J., 2017, *ApJ*, 841, 68
- Vanderbeke J., Baes M., Romanowsky A. J., Schmidtobreck L., 2011, *MNRAS*, 412, 2017
- Vaughan S. P., Houghton R. C. W., Davies R. L., Zieleniewski S., 2018, *MNRAS*, 475, 1073
- Villaume A., Conroy C., Johnson B., Rayner J., Mann A. W., van Dokkum P., 2017, *ApJS*, 230, 23
- Zieleniewski S., Houghton R. C. W., Thatte N., Davies R. L., 2015, *MNRAS*, 452, 597
- Zieleniewski S., Houghton R. C. W., Thatte N., Davies R. L., Vaughan S. P., 2017, *MNRAS*, 465, 192

APPENDIX A: MEASUREMENTS OF ABSORPTION FEATURE INDICES

The full set of measurements for individual galaxies and the stacked spectra are presented in this appendix. These measurements are corrected to 230 km s^{-1} . The velocity dispersions of the *K*-band stacked spectra were measured using pPXF (Cappellari & Emsellem 2004) using the spectral region around the CO bandhead (21 200–23 400 Å). These velocity dispersion measurements are also given in the data tables.

The measured equivalent widths for the KMOS data are presented galaxy by galaxy in Tables A1–A7. The data from the stacked spectra are given in Table A8.

Table A1. A list of index measurements (in Å) for the *K*-band observations of NGC 1407, corrected to 230 km s^{-1} . R1 and R2 correspond to the two extraction regions in the central IFU (<0.7 arcsec, >0.7 arcsec), whilst R3, R4, and R5 correspond to the rings of IFUs arranged at $\sim 1/3 R_{\text{eff}}$, $\sim 2/3 R_{\text{eff}}$, and $\sim R_{\text{eff}}$.

NGC 1407	R1	R2	R3	R4	R5
Ca I 1.98 μm	0.61 ± 4.15	2.53 ± 5.05	-6.46 ± 9.09	-21.67 ± 28.53	29.21 ± 69.27
Na I 2.21 μm	2.75 ± 0.32	2.85 ± 0.98	1.65 ± 0.49	2.39 ± 1.65	-3.21 ± 2.74
Ca I 2.26 μm	3.17 ± 0.65	3.10 ± 1.14	3.67 ± 2.49	1.84 ± 7.82	3.25 ± 5.98
CO 2.30 $\mu\text{m a}$	6.65 ± 0.49	6.82 ± 0.52	6.95 ± 1.88	9.63 ± 9.40	4.91 ± 4.61
CO 2.30 $\mu\text{m b}$	4.36 ± 1.36	8.02 ± 1.44	8.03 ± 5.69	23.71 ± 45.27	6.31 ± 12.01
Average S/N	71	24	33	14	12

Table A2. A list of index measurements (in Å) for the *K*-band observations of NGC 3377, corrected to 230 km s^{-1} . R1 and R2 correspond to the two extraction regions in the central IFU (<0.7 arcsec, >0.7 arcsec), whilst R3, R4, and R5 correspond to the rings of IFUs arranged at $\sim 1/3 R_{\text{eff}}$, $\sim 2/3 R_{\text{eff}}$, and $\sim R_{\text{eff}}$.

NGC 3377	R1	R2	R3	R4	R5
Ca I 1.98 μm	1.13 ± 0.15	0.80 ± 0.20	0.90 ± 0.35	1.42 ± 0.77	0.55 ± 1.11
Na I 2.21 μm	1.73 ± 0.11	1.34 ± 0.22	1.00 ± 0.45	1.89 ± 0.88	3.20 ± 1.39
Ca I 2.26 μm	3.60 ± 0.32	2.41 ± 0.48	3.18 ± 1.65	8.02 ± 2.32	2.37 ± 4.13
CO 2.30 $\mu\text{m a}$	8.33 ± 0.18	7.96 ± 0.21	5.52 ± 1.73	6.23 ± 2.75	2.67 ± 5.15
CO 2.30 $\mu\text{m b}$	6.94 ± 0.20	6.58 ± 0.22	5.58 ± 2.17	376.21 ± 335.59	1.32 ± 5.59
Average S/N	71	24	33	14	12

Table A3. A list of index measurements (in Å) for the *K*-band observations of NGC 3379, corrected to 230 km s^{-1} . R1 and R2 correspond to the two extraction regions in the central IFU (<0.7 arcsec, >0.7 arcsec), whilst R3, R4, and R5 correspond to the rings of IFUs arranged at $\sim 1/3 R_{\text{eff}}$, $\sim 2/3 R_{\text{eff}}$, and $\sim R_{\text{eff}}$.

NGC 3379	R1	R2	R3	R4	R5
Ca I 1.98 μm	1.37 ± 0.22	1.31 ± 0.84	0.96 ± 0.10	0.70 ± 0.15	0.81 ± 0.23
Na I 2.21 μm	2.26 ± 0.18	2.01 ± 0.93	1.67 ± 0.20	1.39 ± 0.44	1.39 ± 0.78
Ca I 2.26 μm	3.60 ± 0.29	3.61 ± 0.77	3.80 ± 0.46	3.26 ± 1.04	2.71 ± 1.83
CO 2.30 $\mu\text{m a}$	8.73 ± 0.10	8.38 ± 0.20	7.29 ± 0.41	7.07 ± 1.04	8.40 ± 1.54
CO 2.30 $\mu\text{m b}$	6.24 ± 0.15	5.91 ± 0.27	5.29 ± 0.58	4.79 ± 1.66	5.47 ± 2.69
Average S/N	71	24	33	14	12

Table A4. A list of index measurements (in Å) for the *K*-band observations of NGC 4486, corrected to 230 km s^{-1} . R1 and R2 correspond to the two extraction regions in the central IFU (<0.7 arcsec, >0.7 arcsec), whilst R3, R4, and R5 correspond to the rings of IFUs arranged at $\sim 1/3 R_{\text{eff}}$, $\sim 2/3 R_{\text{eff}}$, and $\sim R_{\text{eff}}$.

NGC 4486	R1	R2	R3	R4	R5
Ca I 1.98 μm	2.17 ± 2.97	1.74 ± 0.22	2.09 ± 0.27	1.23 ± 0.40	1.48 ± 0.88
Na I 2.21 μm	1.83 ± 1.33	1.85 ± 0.19	2.48 ± 0.32	1.16 ± 0.66	1.46 ± 0.98
Ca I 2.26 μm	2.10 ± 0.79	3.93 ± 0.44	3.97 ± 1.01	2.79 ± 1.91	2.32 ± 3.34
CO 2.30 $\mu\text{m a}$	5.20 ± 0.42	7.47 ± 0.30	9.16 ± 0.90	8.40 ± 1.77	8.54 ± 3.20
CO 2.30 $\mu\text{m b}$	4.42 ± 0.43	5.82 ± 0.37	7.53 ± 1.11	5.01 ± 2.06	7.50 ± 3.44
Average S/N	71	24	33	14	12

Table A5. A list of index measurements (in Å) for the *K*-band observations of NGC 4552, corrected to 230 km s^{-1} . R1 and R2 correspond to the two extraction regions in the central IFU (<0.7 arcsec, >0.7 arcsec), whilst R3, R4, and R5 correspond to the rings of IFUs arranged at $\sim 1/3 R_{\text{eff}}$, $\sim 2/3 R_{\text{eff}}$, and $\sim R_{\text{eff}}$.

NGC 4552	R1	R2	R3	R4	R5
Ca I 1.98 μm	2.96 ± 0.27	3.01 ± 0.29	1.79 ± 0.28	0.23 ± 0.64	0.59 ± 0.70
Na I 2.21 μm	2.29 ± 0.21	2.15 ± 0.25	1.22 ± 0.37	1.72 ± 0.85	1.93 ± 1.03
Ca I 2.26 μm	3.44 ± 0.27	3.26 ± 0.26	2.34 ± 0.98	3.31 ± 2.01	3.59 ± 2.63
CO 2.30 $\mu\text{m a}$	8.39 ± 0.33	8.14 ± 0.31	6.61 ± 0.85	6.58 ± 1.77	8.15 ± 2.50
CO 2.30 $\mu\text{m b}$	6.55 ± 0.16	6.71 ± 0.15	5.78 ± 0.94	7.16 ± 2.12	6.11 ± 2.96
Average S/N	71	24	33	14	12

Table A6. A list of index measurements (in Å) for the *K*-band observations of NGC 4621, corrected to 230 km s^{-1} . R1 and R2 correspond to the two extraction regions in the central IFU ($<0.7 \text{ arcsec}$, $>0.7 \text{ arcsec}$), whilst R3, R4, and R5 correspond to the rings of IFUs arranged at $\sim 1/3 R_{\text{eff}}$, $\sim 2/3 R_{\text{eff}}$, and $\sim R_{\text{eff}}$.

NGC4621	R1	R2	R3	R4	R5
Ca I 1.98 μm	0.16 ± 0.23	0.44 ± 0.52	0.09 ± 0.22	0.54 ± 0.40	1.34 ± 0.48
Na I 2.21 μm	3.31 ± 0.28	2.73 ± 0.53	2.18 ± 0.52	0.66 ± 1.06	1.77 ± 1.67
Ca I 2.26 μm	2.69 ± 0.26	2.15 ± 0.59	1.83 ± 1.32	1.62 ± 2.56	2.66 ± 4.87
CO 2.30 $\mu\text{m } a$	8.57 ± 0.41	8.35 ± 0.47	7.62 ± 1.30	8.26 ± 3.05	105.53 ± 33.77
CO 2.30 $\mu\text{m } b$	7.64 ± 0.24	7.06 ± 0.35	6.70 ± 1.81	6.34 ± 4.95	7.12 ± 73.43
Average S/N	71	24	33	14	12

Table A7. A list of index measurements (in Å) for the *K*-band observations of NGC 5813, corrected to 230 km s^{-1} . R1 and R2 correspond to the two extraction regions in the central IFU ($<0.7 \text{ arcsec}$, $>0.7 \text{ arcsec}$), whilst R3, R4, and R5 correspond to the rings of IFUs arranged at $\sim 1/3 R_{\text{eff}}$, $\sim 2/3 R_{\text{eff}}$, and $\sim R_{\text{eff}}$.

NGC5813	R1	R2	R3	R4	R5
Ca I 1.98 μm	1.86 ± 0.65	2.27 ± 0.78	3.86 ± 3.59	5.98 ± 4.70	1.29 ± 12.11
Na I 2.21 μm	1.94 ± 0.27	1.97 ± 0.65	1.71 ± 1.32	1.05 ± 1.98	2.98 ± 4.11
Ca I 2.26 μm	3.40 ± 0.41	3.35 ± 0.72	1.19 ± 3.34	3.67 ± 5.30	3.60 ± 8.98
CO 2.30 $\mu\text{m } a$	6.84 ± 0.39	7.02 ± 0.46	7.64 ± 2.94	8.43 ± 5.21	0.40 ± 10.77
CO 2.30 $\mu\text{m } b$	6.41 ± 1.31	6.18 ± 1.34	4.58 ± 10.22	7.50 ± 14.47	15.56 ± 36.31
Average S/N	71	24	33	14	12

Table A8. A list of index measurements (in Å) for the stacked spectra, corrected to 230 km s^{-1} . N.B. ‘noise’ in S/N calculation represents scatter between input spectra, not the formal flux uncertainty (which is much lower). This S/N distribution is strongly skewed (e.g. 95 per cent range of central stack is 20–1780). R1 and R2 correspond to the two extraction regions in the central IFU ($<0.7 \text{ arcsec}$, $>0.7 \text{ arcsec}$), whilst R3, R4, and R5 correspond to the rings of IFUs arranged at $\sim 1/3 R_{\text{eff}}$, $\sim 2/3 R_{\text{eff}}$, and $\sim R_{\text{eff}}$.

Stacks	R1	R2	R3	R4	R5
Ca I 1.98 μm	0.44 ± 0.22	0.40 ± 0.12	0.48 ± 0.12	0.53 ± 0.21	0.37 ± 0.30
Na I 2.21 μm	1.82 ± 0.14	1.98 ± 0.05	1.63 ± 0.16	0.96 ± 0.24	0.94 ± 0.30
Ca I 2.26 μm	2.94 ± 0.11	2.87 ± 0.07	2.74 ± 0.16	3.12 ± 0.33	2.73 ± 0.45
CO 2.30 $\mu\text{m } a$	7.14 ± 0.15	7.45 ± 0.06	7.27 ± 0.21	7.13 ± 0.33	5.99 ± 0.64
CO 2.30 $\mu\text{m } b$	5.45 ± 0.21	5.98 ± 0.05	6.34 ± 0.24	5.56 ± 0.48	6.42 ± 0.61
$\sigma_{\text{stack}} / \text{km s}^{-1}$	199 ± 2	211 ± 1	192 ± 3	166 ± 10	151 ± 14
S/N (68 per cent range)	70–600	170–1210	60–490	30–250	20–160

APPENDIX B: INFERENCE OF THE IMF SHAPE

It is possible to characterize the IMF in a variety of ways. In [Paper I](#), we chose to use the quantity f_{dwarf} , the fractional contribution of dwarf stars to the total light, to parametrize the IMF. This choice was motivated by the linearity of the response of the model equivalent widths to changes in f_{dwarf} , a property not shared by other possible parametrizations such as the fractional contribution of dwarf stars to the total stellar mass, or indeed the IMF power-law slope. Moreover, we found that for the spectral features analysed in [Paper I](#) the strength of IMF-sensitive features was approximately independent of the particular shape of the IMF.

We make a clearer demonstration of this point in [Fig. B1](#). For each of the spectral indices considered in [Paper I](#), we show f_{dwarf} plotted against index strength for a grid of IMFs parametrized according to a two-part broken power law, comprising two sections ($0.08\text{--}0.5 M_{\odot}$ and $0.5\text{--}1.0 M_{\odot}$) with independent power-law slopes $X1$ and $X2$. For this grid $X1$, $X2$ run from 0.5 to 3.5 (where $X1 = X2 = 2.3$ corresponds to the Salpeter IMF).

[Fig. B1](#) shows that, in general, the grids fold up tightly around the linear relation we assumed in [Paper I](#) (e.g. Na I 0.82 μm , Na I 1.14 μm , and Ca II triplet). The parameters $X1$ and $X2$ have some

degeneracy and feature strengths principally track f_{dwarf} . Nevertheless, shape-dependent deviations clearly do matter in some cases (e.g. FeH 0.99 μm and H β strength can both vary by $\lesssim 10$ per cent at fixed f_{dwarf}). It is also noteworthy that for bottom-light IMFs (lower fraction of dwarf stars than the Milky Way case, which can be approximated as $X1 = 1.3$, $X2 = 2.3$) the linear relation tends not to be a good model. However, in different wavelength regimes, different stars dominate the total luminosity. One way to extract more information about the detailed shape of the IMF may be to consider spectral indices over a long wavelength range. In [Fig. B2](#), a similar set of relationships to those depicted in [Fig. B1](#) are shown for four *K*-band ($\sim 2 \mu\text{m}$) spectral features; all of these have significant sensitivity to the IMF and all apart from Na I 2.21 μm have a fairly strong dependence on the IMF shape.

This suggests that with a sufficiently wide range of spectral feature measurements, we may be able to recover some information about the shape of the IMF, or else at least should marginalize over reasonable variations in shape to ensure that we obtain robust results. We therefore model the measured features with a broken power law as just described, calculating f_{dwarf} post hoc. When necessary to discuss our inference of the IMF shape, we use the quantity $X2 - X1$, which (as described in [Section 6.3](#)) varies approximately independently of f_{dwarf} in the CvD16 models.

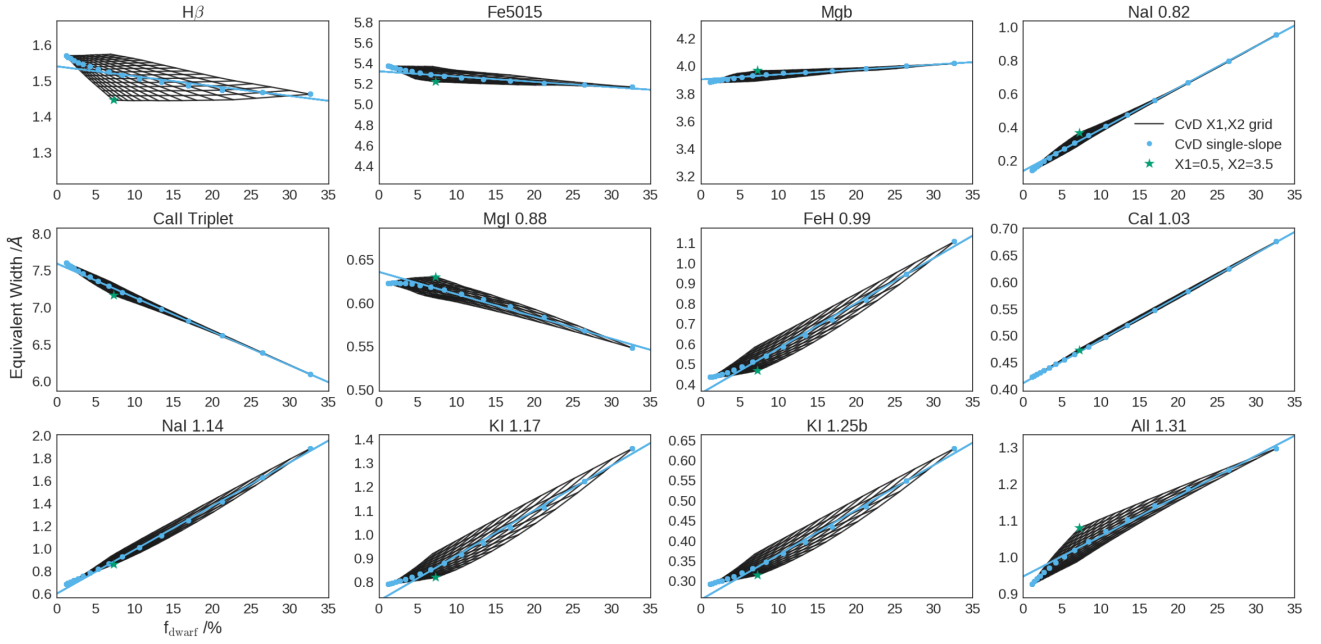


Figure B1. A set of spectral indices, computed for a flexible two-part power-law IMF (described in the text) with slope X_1 below $0.5 M_{\odot}$ and X_2 above. Units are index equivalent width in \AA . The black grid shows the predictions of the model, assuming various combinations of values for X_1 and X_2 between 0.5 and 3.5. The blue points mark the diagonals of the grid ($X_1 = X_2$, the single power-law case) and the blue line is a linear fit to these points for $f_{\text{dwarf}} > 5$ per cent. In each panel, the most convex IMF is marked with a green star.

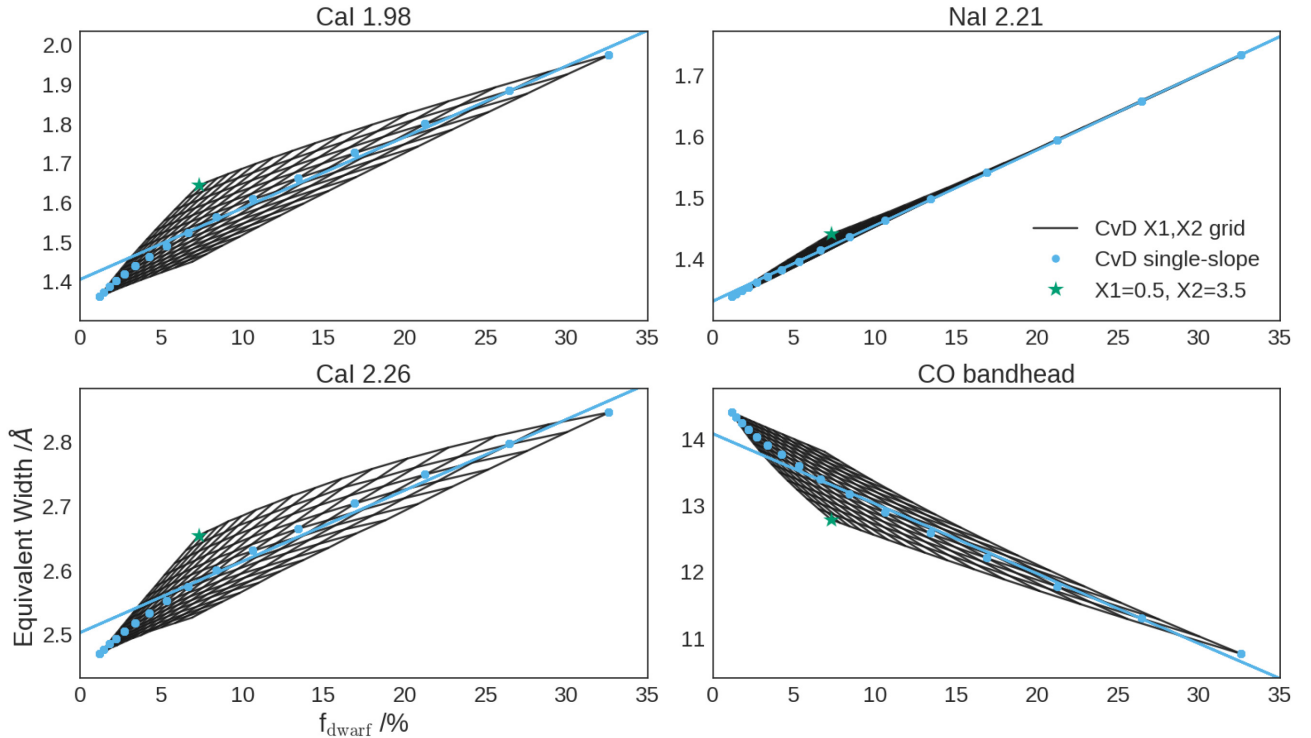


Figure B2. Four K -band spectral indices, computed for a flexible two-part power-law IMF (described in the text). Units are index equivalent widths in \AA . In this case, some indices have non-negligible dependence on the detailed IMF shape: the one-to-one relationship between f_{dwarf} and feature strength given by the blue line only holds strongly for Na I 2.21 μm . In each panel, the most convex IMF is marked with a green star.

This paper has been typeset from a $\text{\TeX}/\text{\LaTeX}$ file prepared by the author.